



저작자표시-비영리-변경금지 2.0 대한민국

이용자는 아래의 조건을 따르는 경우에 한하여 자유롭게

- 이 저작물을 복제, 배포, 전송, 전시, 공연 및 방송할 수 있습니다.

다음과 같은 조건을 따라야 합니다:



저작자표시. 귀하는 원저작자를 표시하여야 합니다.



비영리. 귀하는 이 저작물을 영리 목적으로 이용할 수 없습니다.



변경금지. 귀하는 이 저작물을 개작, 변형 또는 가공할 수 없습니다.

- 귀하는, 이 저작물의 재이용이나 배포의 경우, 이 저작물에 적용된 이용허락조건을 명확하게 나타내어야 합니다.
- 저작권자로부터 별도의 허가를 받으면 이러한 조건들은 적용되지 않습니다.

저작권법에 따른 이용자의 권리는 위의 내용에 의하여 영향을 받지 않습니다.

이것은 [이용허락규약\(Legal Code\)](#)을 이해하기 쉽게 요약한 것입니다.

[Disclaimer](#)

**Master's Thesis of Engineering**

**A Framework for Frequent Multi-  
beam Laser Scanner Self-  
Calibration Using Mobile Mapping  
System Scan Data**

모바일매핑시스템 스캔 데이터를 이용한  
멀티빔레이저스캐너의 지속적  
셀프캘리브레이션 프레임워크

**February 2020**

**Department of Civil and Environmental  
Engineering  
Seoul National University**

**Hansae Kim**

# Abstract

LiDAR (Light Detection and Ranging) sensors provide a more efficient means to acquire accurate 3D information from large-scale environments. Over time, these sensors have become more compact, portable, and readily applicable to mobile applications such as mobile mapping, autonomous vehicle, and robotics. From the variety of LiDAR sensors, multi-beam laser scanners are particularly advantages due to their relatively cheap price and compact size compared to terrestrial laser scanners. As a result, multi-beam laser scanners are one of the most extensively applied scanners for mobile applications.

Despite the efficiency of these scanners, their point cloud accuracy is relatively low to be used effectively in mobile mapping applications which require measurements at a higher level of accuracy. Moreover, multi-beam laser scanners have been reported to be unstable in their system of measurement. To overcome these limitations, various studies have performed self-calibration to reduce the 3D Root Mean Square Error (RMSE) of measurements to sub-centimeter levels. However, results from stability analysis of multi-beam laser scanners indicated that periodic recalibration is necessary to maintain a high level of accuracy. Therefore, frequent *in situ* calibration can be an essential step during the scanner's data acquisition in order to meet the accuracy level requirements and to implement these scanners for precise mobile applications.

This thesis proposes a framework consisting of frequent *in situ* self-calibration of a multi-beam laser scanner using scan data acquired by a Mobile Mapping System (MMS). First, plane-based self-calibration is investigated to perform rigorous calibration. Plane-based self-calibration is widely adopted in *in situ* calibration since planar features are one of the most common geometrical features. Second, after analyzing the functional dependence of the calibration parameters, simulated datasets with various conditions are designed to analyze the impact of the plane's dimension, number of planar features, multiple scans, and network geometry in the adjustment. Third, a calibration dataset acquisition method is proposed by analyzing the experimental results. Finally, a framework for frequent *in situ* self-calibration is proposed and validated using both simulated and real datasets.

The results demonstrated that the proposed framework for multi-beam laser scanner reduced RMSE by 57% when using the real dataset, confirming the framework can be used for indoor mapping where planar features are commonly found. In addition, this method has potential to be adopted during on-line point cloud registration by performing frequent calibration using the MMS scan data.

**Keyword:** LiDAR, self-calibration, multi-beam laser scanner, mobile mapping system

**Student Number:** 2018-24869

# Table of Contents

<b>1. Introduction .....</b>	<b>1</b>
1.1. Necessity of LiDAR Self-Calibration .....	3
1.2. Related Works .....	7
1.2.1. Point-based Method.....	7
1.2.2. Plane-based Method .....	9
1.2.3. Other Method.....	11
1.2. Objectives of the Study .....	12
<b>2. Theoretical Background.....</b>	<b>14</b>
2.1. Sensor Specifications .....	14
2.2. Mathematical Models.....	16
2.2.1. Point Observation Model.....	16
2.2.2. Systematic Error Model.....	18
2.2.3. Plane-based Functional Model .....	22
2.2.4. Least Squares Solution.....	24
<b>3. Functional Dependence of the Calibration Parameters.....</b>	<b>26</b>
3.1. Linear Dependence of the Columns of the Design Matrix....	26
3.2. Analysis of the Partial Derivatives.....	28

3.2.1. Dependence between APs.....	28
3.2.2. Dependence between EOPs.....	30
3.2.3. Dependence between EOPs and APs.....	31
3.3. Summary of the Section .....	33
<b>4. Analysis through Experiments.....</b>	<b>35</b>
4.1. Experimental Design.....	35
4.2. Impact Analysis.....	39
4.2.1. Using Tilted Scan .....	39
4.2.2. Width of Plane .....	44
4.2.3. Number of Incorporated Planes.....	49
4.2.4. Network Geometry .....	54
4.2.5. Number of Incorporated Scans.....	59
4.3. Summary of the Section .....	64
<b>5. Proposed Self-Calibration Framework.....</b>	<b>65</b>
5.1. Self-Calibration Framework.....	65
5.2. Experiment Description .....	68
5.2.1. Simulated Datasets .....	68
5.2.2. Real Dataset.....	71

<b>6. Results and Analysis</b> .....	75
6.1 Calibration Results with Simulated Datasets.....	75
6.2 Calibration Results with Real Dataset .....	82
<b>7. Conclusion</b> .....	86
<b>References</b> .....	88
<b>Abstract in Korean</b> .....	97

## List of Tables

Table 2-1. Specifications of Velodyne VLP-16.....	15
Table 2-2. Summary of Least Squares Solution.....	25
Table 4-1. Average AP Values Used in this Research.....	37
Table 4-2. Summary of Simulated Datasets.....	37
Table 4-3. RMSE of AP Values in Calibration S-I.....	40
Table 4-4. RMSE of AP Values in Calibration S-II.....	45
Table 4-5. RMSE of AP Values in Calibration S-III.....	50
Table 4-6. RMSE of AP Values in Calibration S-IV.....	55
Table 4-7. RMSE of AP Values in Calibration S-V.....	60
Table 5-1. Summary of Calibration Using the Real Dataset.....	73
Table 6-1. Statistics of Planar Misclosure of Proposed Self-Calibration Approach.....	76
Table 6-2. Mean Absolute Difference between Estimated Parameters and Preset Values of Calibration SP-I.....	76
Table 6-3. Averaged Correlation Coefficients Between Estimated Parameters of Calibration SP-I.....	78
Table 6-4. Summary of Planar Misclosure.....	82
Table 6-5. Averaged Correlation Coefficients Between Estimated	

Parameters of Calibration R-I.....	84
Table 6-6. Statistics of the Estimated Parameters of Calibration R-I.....	85

## List of Figures

Figure 1-1. Planar Misclosure Due to Systematic Errors of Multi Laser Scanner VLP-16 (Color Coded by Intensity) .....	6
Figure 2-1. Velodyne VLP-16.....	15
Figure 2-2. VLP-16 Sensor Coordinate System.....	16
Figure 2-3. Additional Parameters of VLP-16.....	19
Figure 2-4. Distortions due to Systematic Errors (Top View) .....	21
Figure 4-1. Simulated Datasets.....	38
Figure 4-2. Calibration Results of Calibration S-I.....	43
Figure 4-3. Calibration Results of Calibration S-II.....	48
Figure 4-4. Overview of Calibration S-III (Labeled number indicates used planes in calibration) .....	50
Figure 4-5. Calibration Results of Calibration S-III.....	53
Figure 4-6. Overview of Calibration S-IV.....	55
Figure 4-7. Calibration Results of Calibration S-IV.....	58
Figure 4-8. Calibration Results of Calibration S-V.....	63
Figure 5-1. Flow chart of Proposed Self-Calibration Framework.....	67
Figure 5-2. Simulated Indoor Environment and Scan Locations.....	69
Figure 5-3. Generated Point Cloud.....	70

Figure 5-4. Calibration Dataset and Matched Planes.....	70
Figure 5-5. Backpack Platform Sensor System.....	72
Figure 5-6. Acquisition Site of the Real Dataset.....	73
Figure 5-7. Point Cloud of Real Dataset Captured at Two Epochs.....	74
Figure 6-1. Planar Misclosure of Proposed Self-Calibration Approach.....	75
Figure 6-2. Measurement Residuals and Range RMSE.....	77
Figure 6-3. Top View of Point Cloud Before (Upper) and After (Lower) Adjustment.....	79
Figure 6-4. Close-up of the Calibration Result (True planes are represented by white lines) .....	80
Figure 6-5. Estimated Planes Before and After Adjustment.....	81
Figure 6-6. Planar Misclosure.....	83
Figure 6-7. Residuals of the Adjustment.....	83

# 1. Introduction

Over the past few years, significant developments of laser scanning technology have increased the feasibility of acquiring large amounts of accurate geometric 3D data. The demand for 3D observations have increased as well with the development of automatic digital image analysis, namely artificial intelligence. In this context, laser scanners have become fundamental mean to acquire 3D information in accordance to the growing demand in this field (Bosché *et al.*, 2015). This trend is particularly relevant in civil engineering, robotics, and computer vision due to the high usage of laser scanners as routine measurement techniques for applications such as 3D modeling and mapping (Cole and Newman, 2006; Wu *et al.*, 2009), efficient building management (Shih *et al.*, 2006; Tang *et al.*, 2011), and transformation of structural health monitoring (Park *et al.*, 2007; Yang *et al.*, 2015). Extending the application of laser scanners from geomatics to these domains has resulted in the emergence of new areas for potential implementation, which require the development of more efficient and accurate acquisition systems (Riveiro and Lindenbergh, 2019).

More recently, Light Detection and Ranging sensor (LiDAR) has become more portable, compact, and readily available to be utilized in mobile applications (Kukko *et al.*, 2012). The advancement of modern

technology has expanded the use of LiDAR sensors to a variety of applications including data collection via various platforms, mobile mapping, and autonomous vehicles. In particular, multi-beam laser scanners are the most extensively used and favored LiDAR sensors for mobile applications because the sensors are relatively lightweight, compact, and cheap. The Velodyne LiDAR is one of the most popular multi-beam laser scanners and has been widely used in the literature and in the industry (Halterman and Bruch, 2010; Moosmann and Stiller, 2011; Geiger *et al.*, 2012; Choi, 2014; Jozkow *et al.*, 2016; Chen *et al.*, 2015; Hess *et al.*, 2016; Ravi *et al.*, 2018; Shamseldin *et al.*, 2018). In more detail, Geiger *et al.* (2012) acquired point cloud data using Velodyne HDL-64E to establish their KITTI benchmark dataset on autonomous driving vehicle platform. In addition, Hess *et al.* (2016) developed 2D and 3D LiDAR Simultaneous Localization and Mapping (SLAM) also known as Google Cartographer using an indoor mobile mapping backpack system consists of two Velodyne VLP-16 and Inertial Measurement Unit (IMU). Similarly, Shamseldin *et al.* (2018) constructed a sensor system using VLP-16 for their indoor LiDAR Mobile Mapping System (MMS). Extending from backpack, ground vehicle, and robotic platforms, Ravi *et al.* (2018) mounted HDL-32E and VLP-16 on an Unmanned Aerial Vehicle (UAV) and developed their own MMS.

## 1.1. Necessity of LiDAR Self-Calibration

Although multi-beam laser scanners provide a cost-efficient and portable option, they are prone to systematic errors which can affect the overall accuracy of the scanned data. Since each mechanically designed laser measures the range by time-of-flight system and encoder angle, the point cloud inevitably contains systematic errors in range and angle measurements with respect to each laser. These systematic errors can cause translations and rotations in the point cloud data. Figure 1-1 shows geometric distortions induced by systematic errors. As a result, the overall accuracy of the point cloud data needs to be minimized for precise mobile mapping and surveying (Chow, 2018). Moreover, Glennie and Lichti (2011) conducted temporal stability analysis of a multi-beam laser scanner, demonstrating that the measurement stability is slightly higher than the quantization level, which stresses the need for periodic recalibration of the LiDAR sensor to maintain a high level of accuracy.

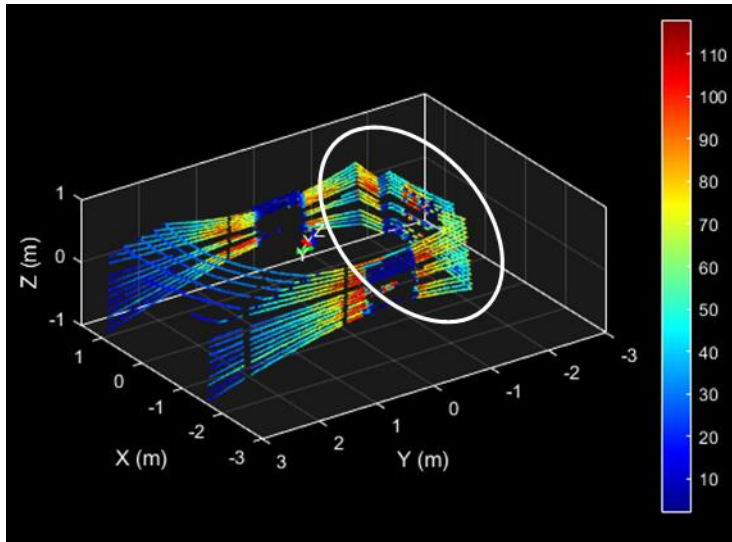
In the computer vision community, research on the optimization of point cloud data has focused on the removal of undesirable data. One of the most frequently used algorithms is RANdom SAMple Consensus (RANSAC). Schnabel *et al.* (2007) proposed RANSAC-based plane detection from point cloud data by removing outliers. Although this

optimization process may exclude extremely inaccurate data, the inliers of the point cloud data may still contain systematic errors.

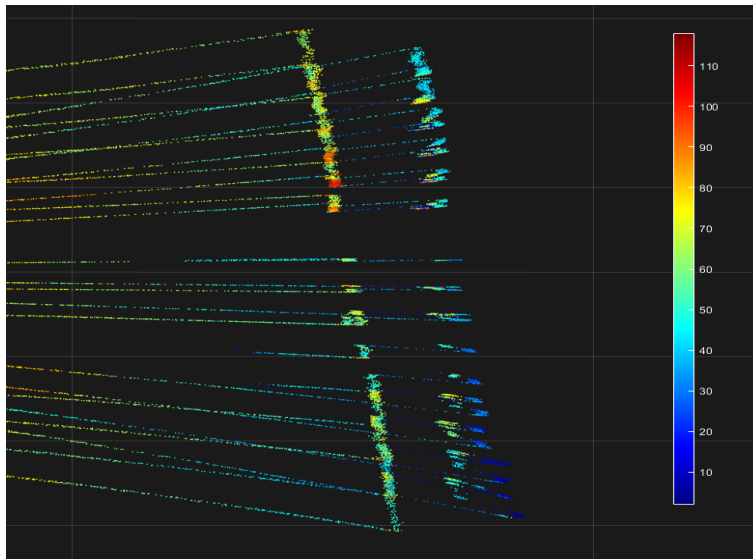
In contrast, self-calibration can reduce the need for outlier removal as a post-processing step and thus improve the overall accuracy of the point cloud measurement by reducing the RMS-error associated with registration and check point (Garcia-San-Miguel and Lerma, 2013). In the field of photogrammetry, self-calibration is defined as the determination of all systematic errors simultaneously with all other system parameters using the concept of additional parameter estimation (Gruen and Beyer, 2001). Based on this definition in relation with laser scanners, self-calibration can be defined as the simultaneous estimation of all systematic errors of a laser scanner in conjunction with all other system parameters (Reshetyuk, Y., 2009). Self-calibration of laser scanners is also often referred to as LiDAR system self-calibration, sensor calibration, and geometric calibration by different researches. The basis of this definition is on the modeling of systematic error with additional parameters.

Various researches in literature have performed self-calibration of multi-beam laser scanners using modified manufacturer-based calibration parameters. Multiple studies confirmed the potential of applying these sensors as a basis towards obtaining a highly accurate mobile mapping platform which showed an improvement from 50 % to 80 % in point cloud accuracy (Glennie and Lichti, 2010; Muhammad and Lacroix, 2010;

Atanacio-Jiménez *et al.*, 2011; Chen *et al.*, 2012). However, the system parameters may still be inconsistent even after self-calibration because of the instability inherent in the measurement scanning system. Instead, self-calibration should be processed during the data acquisition. As a result, periodic *in situ* calibration should be performed to increase and maintain the heightened overall accuracy of the point cloud.



(a) Point Cloud Captured by VLP-16



(b) Planar Misclosure Due to Systematic Errors

**Figure 1-1.** Planar Misclosure Due to Systematic Errors of Multi Laser Scanner VLP-16 (Color Coded by Intensity)

## 1.2. Related Works

Conventional laser scanner self-calibration was conducted using Terrestrial Laser Scanners (TLS), and can be categorized by several methods based on specific conditions to generate a design matrix. Self-calibration can be divided into point- and geometrical feature-based approaches. In general, planar features have been used as geometrical features in self-calibration, which include cylindrical and spherical features. The following sub-sections will cover these self-calibration methods in more detail.

### 1.2.1. Point-based Method

Point-based self-calibration uses center point coordinates extracted from a number of signalized targets through numerous estimation and transformation process (Chow *et al.*, 2010). Chow *et al.* (2010a, 2010b) performed point-based self-calibration using Trimble GS200, GX. Lichti (2010a, 2010b) and Reshetyuk (2010) analyzed the optimal network design for correlation mitigation to achieve good parameterization. Limitations with rigorous *in situ* calibration include manual installation of signalized targets, which is labor-intensive and can decrease the accuracy of point-based self-calibration due to high parameter correlation (Lichti *et*

*al.*, 2011; Chow *et al.*, 2013). Moreover, in the case of multi-beam laser scanners, extracting the exact target points is almost impossible due to its fixed vertical angle.

### 1.2.2. Plane-based Method

Point coordinates on the surface of planar targets can be used directly instead of using center point coordinates of signalized targets. Since signalized targets are not required, plane-based self-calibration is one of the most widely adopted methods. The main advantage of plane-based self-calibration is that the plane parameters within each plane can be estimated in the adjustment model, mitigating the need to measure an accurate reference target and increasing the method's applicability for *in situ* calibration. Skaloud and Lichti (2006) presented a rigorous approach on bore-sight self-calibration in airborne laser scanning system by conditioning the geo-referenced LiDAR points to fit into common plane surfaces. However, the objective of their work was more oriented to estimate extrinsic parameters between the IMU and LiDAR unit, considering only range offset as Additional Parameter (AP). Bae and Lichti (2007) conducted plane-based self-calibration with scan data using FARO 880. Self-calibration simulations investigated various scanner configurations, and results demonstrated that a long baseline between two scan stations enables more accurate estimation of collimation axis errors.

On the other hand, self-calibration using the multi-beam laser scanner, Velodyne HDL-64E, was conducted by Glennie and Lichti (2010) and Muhammad and Lacroix (2010). In the former study, different scan

stations with two fixed stations were used to delineate the scale parameter. In the latter study, precisely designed positional conditions were set to simplify the given cost function. Gerardo *et al.* (2011) placed Velodyne-64E in the center of precisely measured calibration targets. Using pattern planes, ancillary plane orthogonal distance was exploited to minimize planar misclosure using the Levenberg-Marquardt algorithm. Chen and Chien (2012) proposed a fully automated on-site recalibration of Velodyne HDL-64E by linearizing the plane-based functional model. Glennie *et al.* (2016) also conducted calibration and a stability analysis of Velodyne VLP-16 using the same mathematical model used with HDL-64E.

### 1.2.3. Other Method

Chan *et al.* (2015) presented a new cylinder-based self-calibration method which returned higher accuracy and lower correlations between parameters in comparison to plane-based self-calibration.

Overall, previous studies presented rigorous self-calibration approaches to acquire highly accurate 3D information with static sensor stations using signalized targets or geometrical features. One of the key limitations found in previous studies include the fixed positions of two or multiple scan stations, or the precisely measured distance between planes and sensors, which were designed more for a static self-calibration approach. Self-calibration using a known scan location or calibration target may mitigate high correlation among calibration parameters and enhance the accuracy of the adjustment; however, these methods have limitations in *in situ* calibration and periodic recalibration in the case of a LiDAR sensor mounted on an MMS.

### **1.3. Objectives of the Study**

The objectives of this thesis are as follows: (1) to analyze the linear dependence among calibration parameters and evaluate the performance of calibration under various conditions using five experimental setups (refer to Section 4), and (2) to propose a frequent self-calibration framework during data acquisition using conditions which is investigated in (1).

In this thesis, the optimal network design and calibration site is first analyzed by investigating the plane-based functional model and conducting experiments to propose a self-calibration framework using MMS scan data. The functional dependence between Exterior Orientation Parameters (EOP), APs, and Plane Parameters (PP) were analyzed by investigating partial derivatives of the plane-based functional model. Then, the performance of self-calibration was evaluated by simulations designed based on the analysis of the functional model. Simulation tests were conducted for the following advantages. First, LiDAR sensor can be located with exact preset values in the predefined calibration site. That is, all orientation parameters involved in the test can be controlled without any limitations. However, calibration using real data is somewhat limited in accurately positioning the sensor and constructing calibration site due to the error associated with setting each variable. Next, simulations can be

performed after setting all the systematic errors involved in the test. Calibration results can then be directly compared to the preset values, which enables to confirm the accuracy of the adjustment more clearly. Lastly, simulation results can be used to set up the real experiments, reducing the time and economic costs (Choi *et al.*, 2019). After confirming the optimal conditions for calibration, a frequent self-calibration framework is proposed based upon the analysis and the accuracy of the method is evaluated using real datasets captured by backpack platform sensor system.

The remainder of this research thesis is organized as follows. In Section 2, mathematical models of self-calibration used in this study are described. The specifications of the sensor used in this research are also included. In Section 3, partial derivatives of the functional model are examined. Optimal conditions to decorrelate parameters can be found by examining the linear dependence between the columns of the design matrix. Based upon the analysis in Section 3, simulated datasets are designed in Section 4, and self-calibration was conducted to analyze the impact of calibration datasets established under various conditions. Then, in Section 5, a self-calibration framework is proposed where both simulated and real datasets were acquired to validate the framework. Experimental results and analysis are provided in Section 6, followed by the conclusion to this research in Section 7.

## **2. Theoretical Background**

The sensor specifications for Velodyne VLP-16 used in this research and the mathematical models which serve as a theoretical basis are provided in the following sub-sections.

### **2.1. Sensor Specifications**

The multi-beam laser scanner used in this study is Velodyne VLP-16 (Figure 2-1). After its release in 2014, the sensor has been extensively utilized in mobile applications for both research and in the industry. The sensor's specifications are summarized in Table 2-1. The sensor consists of 16 pairs of simultaneously rotating laser emitters and receivers within a compact sensor pod, and each laser has a fixed vertical angle of  $2^\circ$  resolution. The rotation rate varies from 5 Hz to 20 Hz, set with a default value of 10 Hz, which gives  $0.2^\circ$  of horizontal angular resolution. Using default settings, VLP-16 rotates every 0.1 second and acquires approximately 28,800 points for each epoch.



**Figure 2-1.** Velodyne VLP-16

**Table 2-1.** Specifications of Velodyne VLP-16

<b>Category</b>	<b>Specifications</b>
Channels	16 lasers
Range	Up to 100 m
Range Accuracy	Up to $\pm 3$ cm
Field of View (Vertical)	$+15.0^\circ$ to $-15.0^\circ$ ( $30^\circ$ )
Angular Resolution (Vertical)	$2.0^\circ$
Field of View (Horizontal)	$360^\circ$
Angular Resolution (Horizontal/Azimuth)	$0.1^\circ - 0.4^\circ$
Rotation Rate	5 Hz – 20 Hz
Weight	830g
Dimensions	7.2 cm (height) by 10.3cm (diameter)

## 2.2. Mathematical Models

In this section, the point observation model for VLP-16 and the systematic error model for the sensor model are described. Subsequently, the plane-based functional model and adjustment model for self-calibration are provided.

### 2.2.1. Point Observation Model

Since VLP-16 acquires range and horizontal angle measurements, as shown in Figure 2-2, the Cartesian coordinates of the point cloud are calculated by using a Spherical coordinate system, given by Equation 2-1:

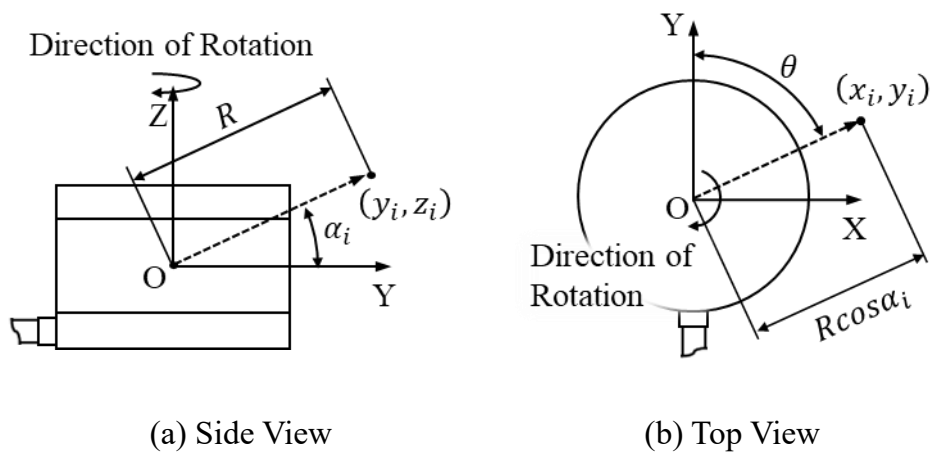


**Figure 2-2.** VLP-16 Sensor Coordinate System

$$\vec{l}_i^n = \begin{bmatrix} x_i^n \\ y_i^n \\ z_i^n \end{bmatrix} = \begin{bmatrix} R \cos \alpha_i^n \sin \theta^n \\ R \cos \alpha_i^n \cos \theta^n \\ R \sin \alpha_i^n \end{bmatrix} \quad (2-1)$$

where,  $\vec{l}_i^n$  is the position of the 3D point for laser  $i$  calculated by nominal vertical and encoder angle measurements,  $R$  is the raw distance measurement,  $\alpha_i^n$  is the nominal fixed vertical angle, and  $\theta^n$  is the nominal encoder angle measurement.

### 2.2.2. Systematic Error Model

Sensor modelling is crucial steps to conduct rigorous self-calibration of laser scanners (Lichti and Licht, 2006; Bae and Lichti, 2007). The error model for laser scanners are well-established as shown in previous studies. Lichti *et al.* (2000) first estimated the error model of a laser scanner and determined accuracies of estimated parameters by comparing measurements with an electronic distance measurement. The final model can be found in Lichti (2007), which consists of about 20 parameters, and is the most widely adopted error model for laser scanner self-calibration.

In the case of multi-beam laser scanners, systematic error coefficients also referred to as APs are defined by six parameters given by the manufacturer to model the deviations of measurements. Among the parameters, horizontal offset and vertical offset are not considered in the adjustment for the following reasons:

(1) Horizontal and vertical offset are highly correlated to the horizontal and vertical rotations, respectively (Glennie and Lichti, 2010; Glennie, 2012). In the case of VLP-16, the correlation coefficients of the parameters corresponding to the vertical and horizontal rotation corrections were found between 0.92 and 0.98, respectively (Glennie *et al.*, 2016).

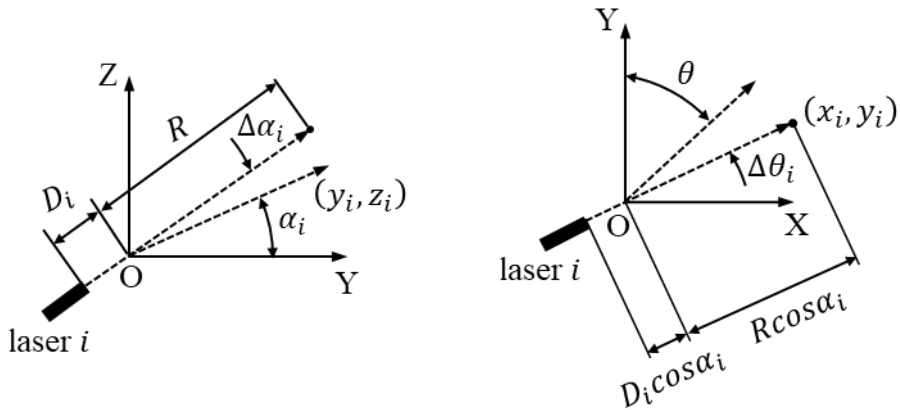
(2) The vertical and horizontal alignments of each laser is precisely located according to manufacturer-provided values set below the accuracy

of the range observation.

(3) Local coordinate error induced by horizontal and vertical offsets are not linearly dependent in the range observation.

Therefore, the horizontal and vertical offsets are fixed to maintain a higher accuracy of calibration.

Ideal 3D points of VLP-16 can be computed by converting from the Spherical to the Cartesian coordinate system, as shown in Figure 2-3 and expressed by Equation (2-2).



(a) Additional Parameters in yz-plane

(b) Additional Parameters in xy-plane

**Figure 2-3.** Additional Parameters of VLP-16

$$\vec{l}_i = \begin{bmatrix} x_i \\ y_i \\ z_i \end{bmatrix} = \begin{bmatrix} (S_i R + D_i) \cos(\alpha_i + \Delta\alpha_i) \sin(\theta + \Delta\theta_i) \\ (S_i R + D_i) \cos(\alpha_i + \Delta\alpha_i) \cos(\theta + \Delta\theta_i) \\ (S_i R + D_i) \sin(\alpha_i + \Delta\alpha_i) \end{bmatrix} \quad (2-2)$$

where,  $R$  = raw distance measurement,  $\theta$  = horizontal angle measurement,  $\alpha_i$  = fixed vertical angle for laser  $i$ ,  $S_i$  = range scale factor for laser  $i$ ,  $D_i$  = range offset for laser  $i$ ,  $\Delta\alpha_i$  = vertical angular offset for laser  $i$ ,  $\Delta\theta_i$  = horizontal angular offset for laser  $i$

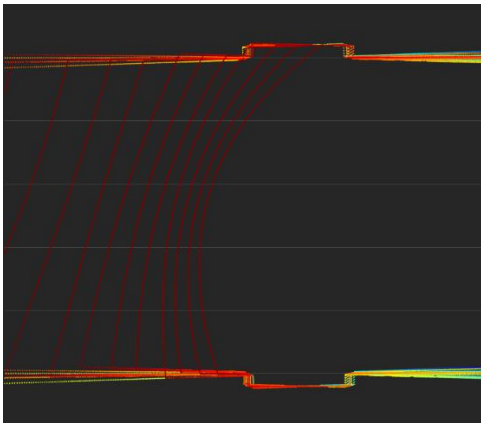
Each AP induces a specific impact on point cloud distortions. Figure 2-4 describes the point cloud distortions due to each AP. The scale factor and angular offsets tend to thicken the planes, while distance offset causes the curve of planes. Horizontal angular offset has impact to thicken the vertical planes and vertical angular offsets thickens the horizontal planes. These systematic error causes overall decrease of point cloud and geometrical features.



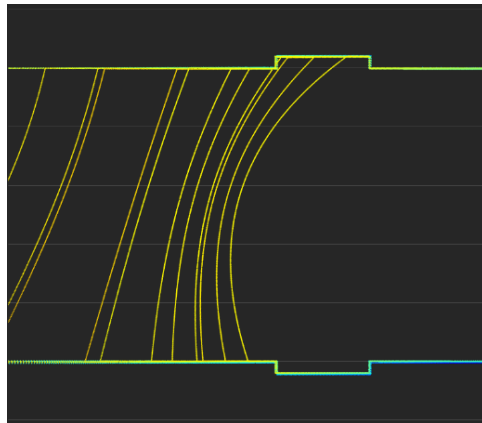
(a) Distortions Due to Scale



(b) Distortions Due to Distance Offset



(c) Distortions Due to Horizontal Angular Offset



(d) Distortions Due to Vertical Angular Offset

**Figure 2-4.** Distortions due to Systematic Errors (Top View)

### 2.2.3. Plane-based Functional Model

The self-calibration approach in this study is based upon a plane-based functional model by Bae and Lichti (2007). This model estimates not only the intrinsic parameters, but also parameters of planar features. This eliminates the need to set up calibration targets and precise specification of planar features using additional sensors. The condition equation associated with EOP, AP, PP, and observation measurements can be expressed by plane-based functional model (Equation 2-3):

$$f(\vec{x}_{EOP_e}, \vec{x}_{PP_k}, \vec{x}_{AP}, \vec{l}_{ijkn}) = [a_c \ b_c \ c_c] \cdot \begin{bmatrix} X_{ijkn} \\ Y_{ijkn} \\ Z_{ijkn} \end{bmatrix} - d_k = 0 \quad (2-3)$$

where  $\vec{x}_{EOP_e}$  denotes Exterior Orientation Parameters (EOP) which are used to transform the local coordinate system of scanner  $j$  to a consistent local coordinate system which defines the datum.  $\vec{x}_{PP_k}$  represents the vector of plane parameters of planar feature  $k$ ,  $\vec{x}_{AP}$  signifies the vector of unknown additional parameters, and  $\vec{l}_{ijkn}$  refers to the vector of LiDAR points  $n$  at epoch  $j$  lying on planar feature  $k$  by laser  $i$  within the local coordinate system.

The  $n^{th}$  point at different epoch  $j$  lying on planar feature  $k$  by laser

$i$  can be calculated by a rigid body transformation in reference epoch coordinate frame as given in Equation (2-4):

$$\begin{bmatrix} X_{ijkn} \\ Y_{ijkn} \\ Z_{ijkn} \end{bmatrix} = R(\omega, \phi, \kappa)_j \vec{l}_{ijkn} + \begin{bmatrix} X_{oj} \\ Y_{oj} \\ Z_{oj} \end{bmatrix} \quad (2-4)$$

where rotation matrix  $R(\omega, \phi, \kappa)_j = \begin{bmatrix} r_{11} & r_{12} & r_{13} \\ r_{21} & r_{22} & r_{23} \\ r_{31} & r_{32} & r_{33} \end{bmatrix}$  and translation

vector  $\begin{bmatrix} X_{oj} & Y_{oj} & Z_{oj} \end{bmatrix}^T$  is between the epoch  $j$  and the locally defined coordinate frame, respectively. Also, the direction cosines of planar feature  $k$  must satisfy the unit length constraint (Equation 2-5):

$$a_k^2 + b_k^2 + c_k^2 - 1 = 0 \quad (2-5)$$

#### 2.2.4. Least Squares Solution

The combined adjustment model (Gauss-Helmert adjustment model) is used since the objective function includes inseparable observations and parameters, and each function includes more than one observation. Details on the implementation of the Gauss-Helmert adjustment model can be found in Skaloud and Lichti (2006). The model minimizes the derivations of the individual LiDAR points of the planar constraints, which is given by Equation (2-3).

In Table 2-2, a summary of the least squares solution is shown. The number of conditions equals the number of points. For the number of observations, a multi-beam laser scanner provides two observations for each point, namely, range and horizontal angle. The number of unknowns can be calculated by summing the number of EOPs, APs, and PPs. Since the reference epoch is fixed to define datum and planar constraints, six EOPs for each additional epoch and four PPs are considered as unknowns defined by the reference epoch. Four APs are considered as unknowns for each laser. However, all 16 laser angular offsets cannot be estimated simultaneously because a certain amount of angular offset for every laser can be compensated by sensor orientation, causing a problem when defining scanner space. Therefore, horizontal and vertical angular offsets for one laser are held fixed.

**Table 2-2.** Summary of Least Squares Solution

<b>Category</b>	<b>No.</b>
Conditions	$m = n$
Unknowns	$u = [6 (\text{epochs} - 1) + 4 (\text{lasers} - 1) + 2] + 4k$
Observations	$l = 2n$
Constraints	$c = k$
Degree of Freedom	$r = n - u + c$

### 3. Functional Dependence of the Calibration Parameters

In order to reduce the functional dependence between model parameters, it is important to analyze the linear dependency between columns of design matrix. In this section, column vectors of the partial derivatives in the design matrix were analyzed by investigating the functional relationship between calibration parameters.

#### 3.1. Linear Dependence of the Columns of the Design Matrix

Let  $A$  be the design matrix of the partial derivatives of the plane-based functional model differentiated with respect to the calibration parameters using  $j$  epochs and  $k$  planar features, and each feature is sampled with the number of points  $i_k$ . Also, let  $\vec{x} = [x_1 \ x_2 \ \cdots \ x_n]^T$  be the unknown vector of the calibration,  $a_t$  be the column of  $A$  associated with an unknown  $x_t$ . Then, these variables can be expressed as shown in Equation (3-1).

$$\vec{a}_{x_t} = \lambda_1 \vec{a}_{x_1} + \lambda_2 \vec{a}_{x_2} + \cdots + \lambda_n \vec{a}_{x_n} \quad (3-1)$$

$\vec{a}_{x_t}$  is linearly dependent on  $a_{x_1}, a_{x_2}, \dots, a_{x_n}$ , if and only if the scalars  $\lambda_1, \lambda_2, \dots, \lambda_n$  are nonzero.  $\vec{a}_{x_t}$  has the following form:

$$\vec{a}_{x_t} = [\vec{p}_{x_t}^{1,1} \vec{p}_{x_t}^{1,2} \dots \vec{p}_{x_t}^{1,i} \vec{p}_{x_t}^{2,1} \vec{p}_{x_t}^{2,2} \dots \vec{p}_{x_t}^{2,i} \vec{p}_{x_t}^{j,1} \vec{p}_{x_t}^{j,2} \dots \vec{p}_{x_t}^{j,i}]^T \quad (3-2)$$

where  $\vec{p}_{x_t}^{j,k} = \left[ \frac{\partial f}{\partial x_t} \Big|_{\vec{l}_{1,j,k}} \frac{\partial f}{\partial x_t} \Big|_{\vec{l}_{2,j,k}} \dots \frac{\partial f}{\partial x_q} \Big|_{\vec{l}_{i_k,j,k}} \right]^T$  and  $\vec{l}$  is the observation vector, while subscripts  $j$  and  $k$  indicate the epoch and the feature number, respectively.

## 3.2. Analysis of the Partial Derivatives

In this section, the partial derivatives of the model with respect to the calibration parameters were analyzed under the assumption that AP terms are assumed to be small. AP terms are therefore neglected in the partial derivative expressions in order to simplify the calculation process.

### 3.2.1. Dependence between APs

The partial derivatives of the model with respect to  $S$  and  $D$  are:

$$\begin{aligned} \frac{\partial f}{\partial S} = & R [a(r_{11} \cos \alpha \sin \theta + r_{12} \cos \alpha \sin \theta + r_{13} \sin \alpha) + \\ & b(r_{21} \cos \alpha \sin \theta + r_{22} \cos \alpha \sin \theta + r_{23} \sin \alpha) + c(r_{31} \cos \alpha \sin \theta + \\ & r_{32} \cos \alpha \sin \theta + r_{33} \sin \alpha)] \end{aligned} \quad (3-3)$$

$$\begin{aligned} \frac{\partial f}{\partial D} = & a(r_{11} \cos \alpha \sin \theta + r_{12} \cos \alpha \sin \theta + r_{13} \sin \alpha) + \\ & b(r_{21} \cos \alpha \sin \theta + r_{22} \cos \alpha \sin \theta + r_{23} \sin \alpha) + c(r_{31} \cos \alpha \sin \theta + \\ & r_{32} \cos \alpha \sin \theta + r_{33} \sin \alpha) \end{aligned} \quad (3-4)$$

It can be seen that the partial derivative of the model with respect to  $S$  and  $D$  have a similar form. The difference is that the  $\frac{\partial f}{\partial S}$  has the form of

$\frac{\partial f}{\partial D}$  multiplied by range observation. Since the direction cosines of the planar models and vertical angle are constant, assuming that the range observation ( $R$ ) is nearly approximated as being constant, partial derivatives of the models with respect to  $S$  can be expressed by:

$$\vec{a}_{x_S} \approx \lambda \vec{a}_{x_D} \quad (3-5)$$

which means  $\vec{a}_{x_S}$  and  $\vec{a}_{x_D}$  can be linearly dependent, thus causing a decrease of overall adjustment accuracy. A variety of range observations is required to avoid linear dependence between two partial derivatives and to increase the overall calibration accuracy.

### 3.2.2. Dependence between EOPs

The partial derivatives of the model with respect to  $X_o$ ,  $Y_o$ , and  $Z_o$  are

$$\frac{\partial f}{\partial X_o} = a \quad (3-6)$$

$$\frac{\partial f}{\partial Y_o} = b \quad (3-7)$$

$$\frac{\partial f}{\partial Z_o} = c \quad (3-8)$$

From the Equations (3-6, 7, and 8), if direction cosines of planes are nearly parallel, linear dependence can be shown by the following expression:

$$\vec{a}_{x_{X_o, Y_o, Z_o}} \approx \lambda_1 \vec{a}_{x_{X_o}} + \lambda_2 \vec{a}_{x_{Y_o}} + \lambda_3 \vec{a}_{x_{Z_o}} \quad (3-9)$$

In this manner, using more planar features with various direction cosines can increase the calibration accuracy. Also, direction cosines must not be zero when estimating  $X_o$ ,  $Y_o$ , and  $Z_o$ . Thus, (1) at least two vertical planes and a horizontal plane, (2) inclined planes, or (3) a tilted scan must be implemented.

### 3.2.3. Dependence between EOPs and APs

Assume that only  $\kappa$  angle has changed with different epochs. Then, partial derivatives of the model with respect to  $\Delta\theta, \Delta\alpha$ , and  $\kappa$  can be simplified by:

$$\frac{\partial f}{\partial \Delta\theta} \approx R[a \cos \alpha \cos(\theta + \kappa) - b \cos \alpha \sin(\theta + \kappa)] \quad (3-10)$$

$$\frac{\partial f}{\partial \Delta\alpha} \approx R[a \sin \alpha \sin(\theta + \kappa) - b \sin \alpha \cos(\theta + \kappa)] \quad (3-11)$$

$$\frac{\partial f}{\partial \kappa} \approx R[a \cos \alpha \sin(\theta + \kappa) + b \cos \alpha \cos(\theta + \kappa)] \quad (3-12)$$

From the above equations, if the horizontal angle observation is approximated as a constant,  $\cos(\theta + \kappa)$  and  $\sin(\theta + \kappa)$  are also approximated as a constant. Then,  $a_{x_{\Delta\theta}}$ ,  $a_{x_{\Delta\alpha}}$ , and  $a_{x_{\kappa}}$  can be highly linearly dependent after factoring out by  $a_{x_{X_0}}$  and  $a_{x_{Y_0}}$ :

$$\vec{a}_{\Delta\theta, \Delta\alpha, \kappa} \approx \lambda_1 \vec{a}_{x_{X_0}} + \lambda_2 \vec{a}_{x_{Y_0}} \quad (3-13)$$

This is only the case when only  $\kappa$  angle has changed, which indicates that no tilted scan is incorporated. Therefore, a variety of horizontal angle

observations and tilted scan with different orientation angles must be incorporated to reduce the linear dependence between EOPs and APs.

### 3.2.4. Summary of the Section

Through analyzing the functional dependence among calibration parameters, following conditions were shown to be helpful for reducing the linear dependence of design matrix.

First, various range observations should be acquired to decorrelate the scale factor and the distance offset. Second, numerous horizontal angle observations are required to reduce the linear dependence between angular offsets and the sensor orientation angle. Furthermore, the range and horizontal angle observations are interrelated in plane-based self-calibration. These observations are dependent on the dimension of the incorporated planar feature. If planar features have a narrow width, range and horizontal angle observations can be approximated as a constant. Therefore, in order to have a variety of range and horizontal angle observations, the dimension of the incorporated planes should be large.

Third, at least one horizontal plane and two vertical planes must be included to estimate  $X_o$ ,  $Y_o$ , and  $Z_o$ . Also, utilizing a larger number of incorporated planes can provide a diversity of condition equations which are needed to reduce correlations between parameters.

Fourth, a tilted scan must be included in the reference epoch to ensure that the direction cosines are nonzero. This step can avoid causing an ill-condition or a singular problem in the adjustment and reduce linear

dependence between angular offsets and sensor orientation angles.

Fifth, at least two epochs must be included in the calibration dataset to provide high redundancy for estimating distance offset and other parameters.

## 4. Analysis through Experiments

### 4.1. Experimental Design

Datasets were simulated under various conditions to evaluate the performance of self-calibration. All datasets were generated with a preset of  $0.2^\circ$  horizontal angle increment and used the same systematic errors with no random noise added. AP values were chosen based upon well-studied literature which used Velodyne HDL-64E (Lichti *et al.*, 2010; Chan *et al.*, 2015). The AP values used in this research are shown in Table 4-1. Simulated datasets are described in Figure 4-1, and the summary of datasets are shown in Table 4-2.

In this section, experiments with simulated datasets were conducted to analyze the impact of various conditions, namely, a tilting angle of the sensor, the dimension of planes, the number of planes, network geometry, and the number of epochs. In Calibration S-I, calibration tests were conducted to analyze the impact of the tilting angle of the sensor's orientation by adjusting the tilting angle with an increment of  $5^\circ$ . In Calibration S-II, along with five planar features already included in the test, the plane widths were expanded by 1m to analyze the impact of the dimension of planar features. In Calibration S-III, calibration was first

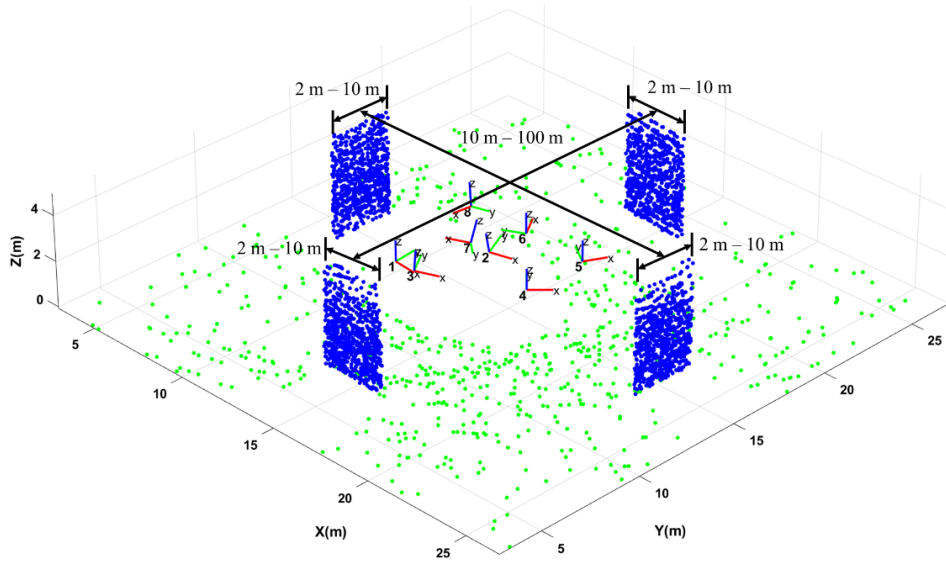
performed using one horizontal plane and two vertical planes, and then repeated six times using one more vertical plane successively. In Calibration S-IV, the second sensor location was moved toward the planes by approximately 1m to analyze the impact of using a variety of range observations. In Calibration S-V, adjustments were conducted seven times by successively incorporating one more epoch with different locations and orientations to analyze the impact of using multiple epochs.

**Table 4-1.** Average AP Values Used in this Research

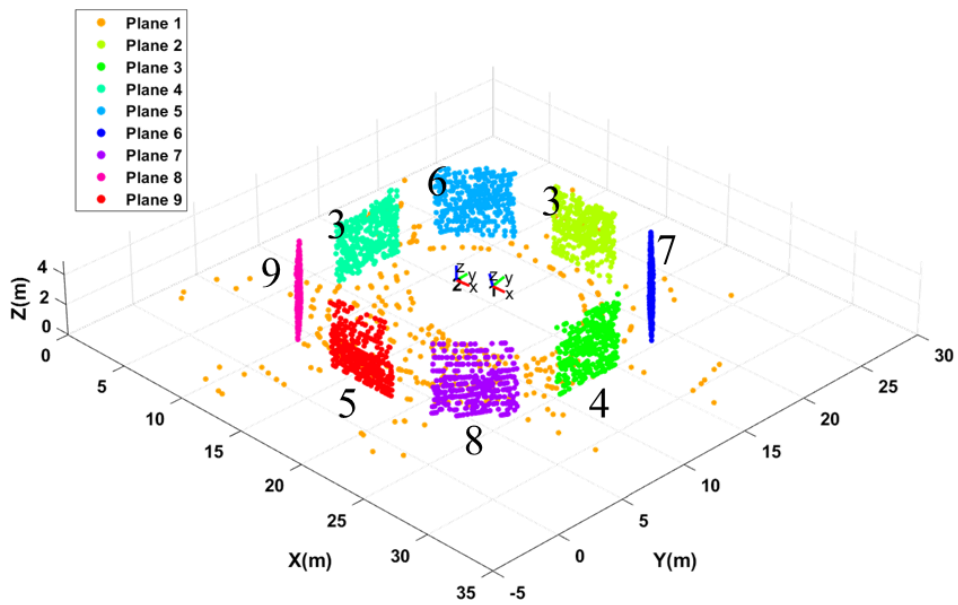
<b>AP</b>	<b>Value</b>
$S$	0.0005
$D$ (m)	0.06
$\Delta\theta$ (deg)	0.05
$\Delta\alpha$ (deg)	0.1

**Table 4-2.** Summary of Simulated Datasets

<b>Calibration</b>	<b>Conditions</b>	<b>No. of Epochs</b>	<b>No. of Planar Features</b>	<b>Tilted Angle (deg)</b>	<b>No. of Points Used</b>
S-I	Tilted Angle	2	5	0 – 25	4096
S-II	Width of Plane	2	5	15	4096
S-III	No. of Planes	2	3 – 9	15	4096
S-IV	Network Geometry	2	5	15	4096
S-V	No. of Epochs	2-8	5	15	4090



(a) Simulated Dataset for Calibration S-I, II, IV, V



(b) Simulated Dataset for Calibration S-III

**Figure 4-1.** Simulated Datasets

## 4.2. Impact Analysis

Calibration tests were performed using each dataset given in Table 4-2. In performing the tests, however, if scale factor, sensor location, and orthogonal distance between sensor location and plane are estimated simultaneously, a global minimum can be reached where the objective function is approximated as being nearly zero (Chen *et al.*, 2012). As a result, since there are no *a priori* known locations of the targets or the scanner, the scale factor was held fixed at 1, while only the distance offset as well as the horizontal and vertical angular offsets were considered as APs.

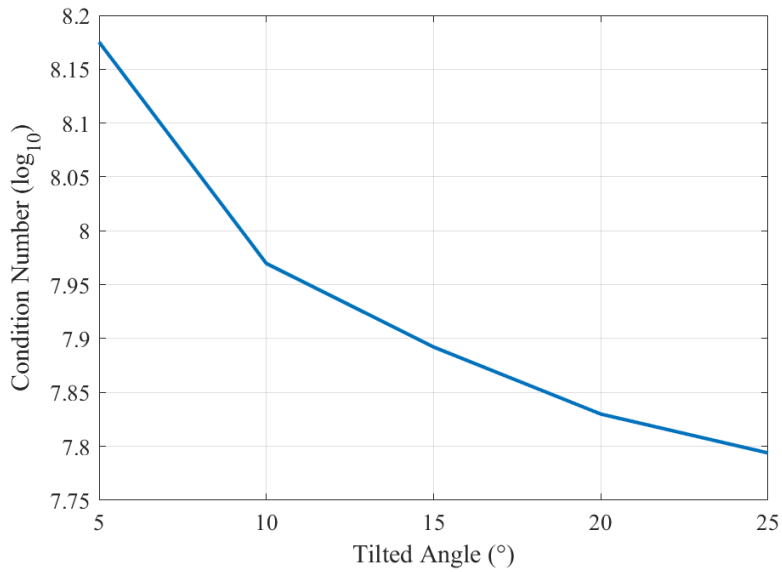
### 4.2.1. Using Tilted Scan

The impact of using a tilting angle of sensor orientation was analyzed in Calibration S-I. Scanner orientation angle ( $\omega$ ) was firstly set to perfectly levelled and increased by  $5^\circ$  for successive tests. As shown in Table 4-3, a perfectly leveled scan with no tilted scan caused an ill-condition problem and the RMSE of AP values were found at a minimum around  $10^\circ$  to  $15^\circ$  of orientation angle. Figure 4-2(a) shows a higher tilting angle results in lower condition numbers whereas Figure 4-2(b)-(f) do not show clear tendency of more accurate calibration results. As tilting angle ( $\omega$ )

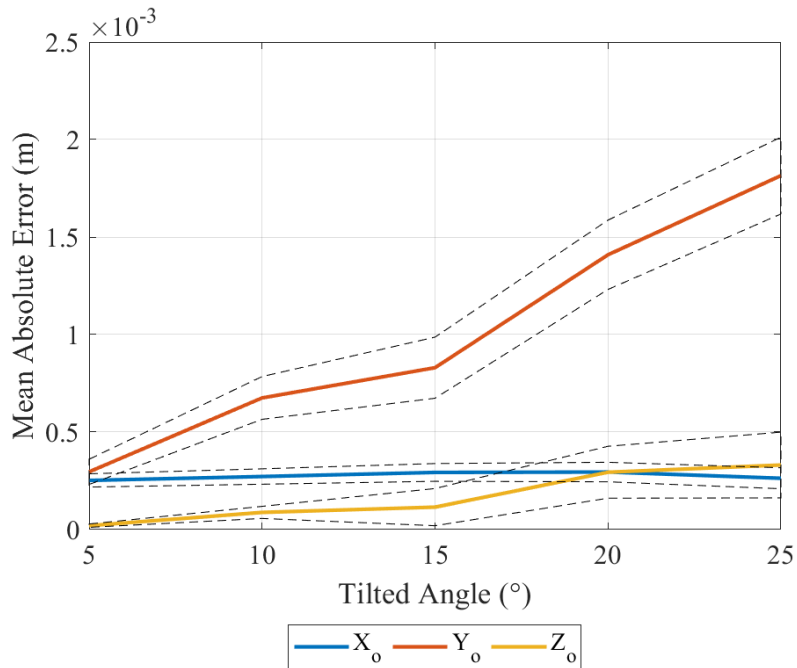
increases, Mean Absolute Error (MAE) of  $Y_o$  and  $Z_o$  increased (Figure 4-2(b)) and corresponding orientation angle parameter showed significantly higher MAE (Figure 4-2(c)). RMSE of the distance offset parameter showed the highest value at  $15^\circ$  of tilted angle, while the vertical angular offset showed the lowest RMSE (Figure 4-2(d) and (e)). The precision of the calibration parameters slightly increased as the tilting angle increases. Hence, the tilting angle should not be large, as the accuracy of EOPs can be lower as tilting angle increases.

**Table 4-3.** RMSE of AP Values in Calibration S-I

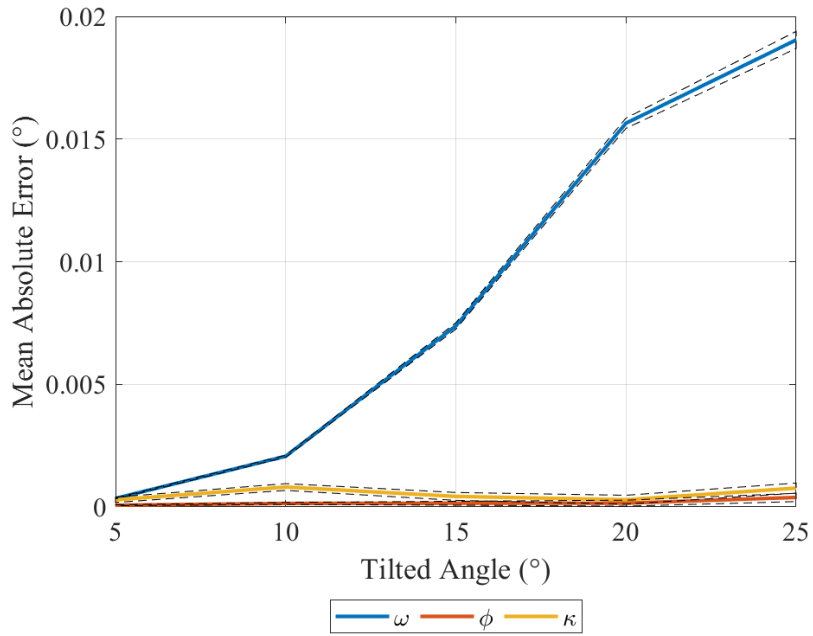
<b>Tilted Angle (<math>^\circ</math>)</b>	<b><math>D</math> (m)</b>	<b><math>\Delta\theta</math> (deg)</b>	<b><math>\Delta\alpha</math> (deg)</b>
0		Ill-conditioned	
5	0.005	0.001	0.017
10	0.005	0.002	0.006
15	0.006	0.002	0.005
20	0.006	0.001	0.009
25	0.005	0.001	0.011



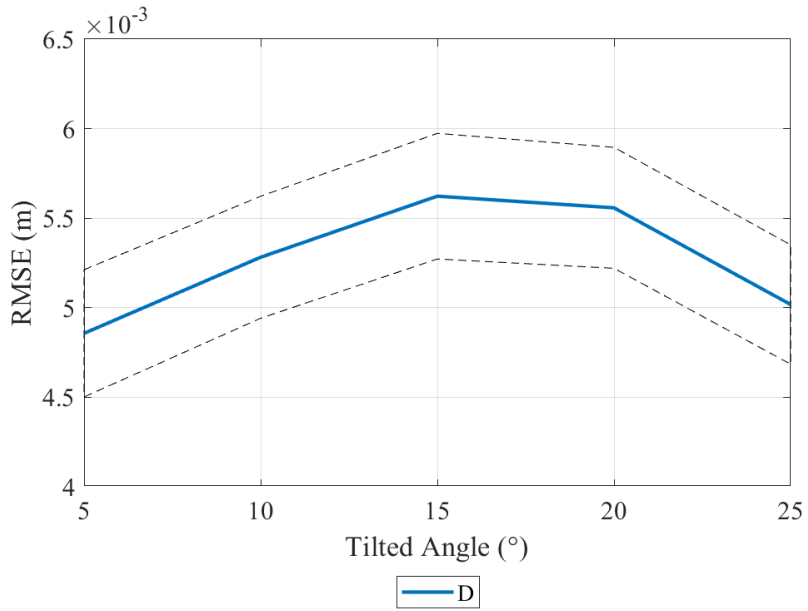
(a) Condition Number of Design Matrix



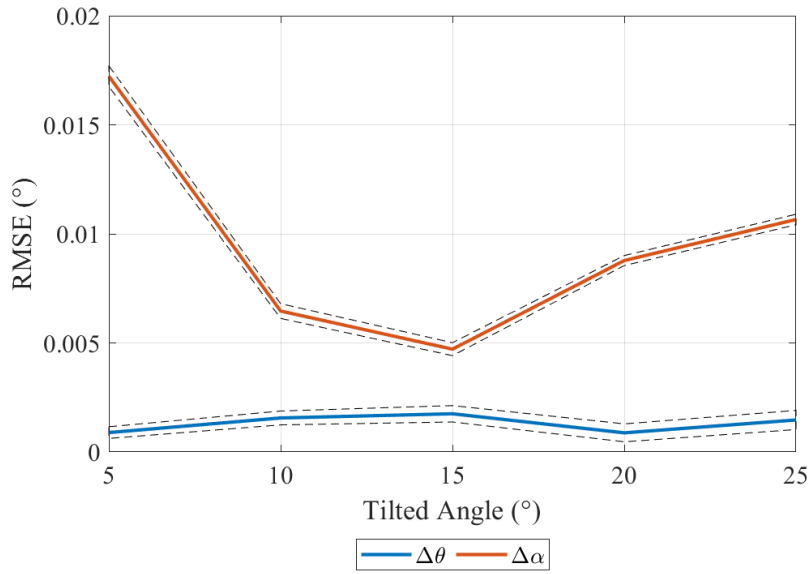
(b) MAE of Scanner Position Parameters



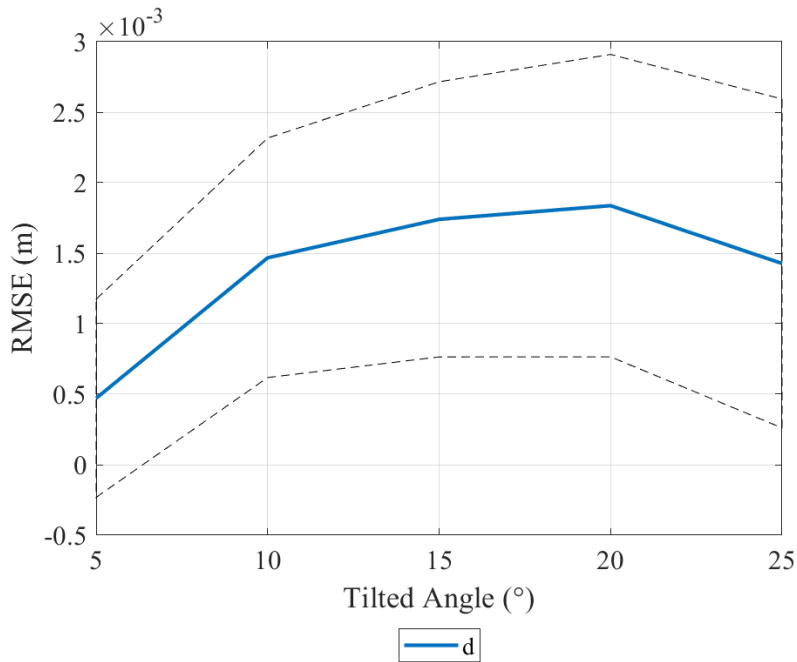
(c) MAE of Scanner Orientation Parameters



(d) RMSE of Distance Offset



(e) RMSE of Angular Offsets



(f) Distance between Scanner and Planes

**Figure 4-2.** Calibration Results of Calibration S-I

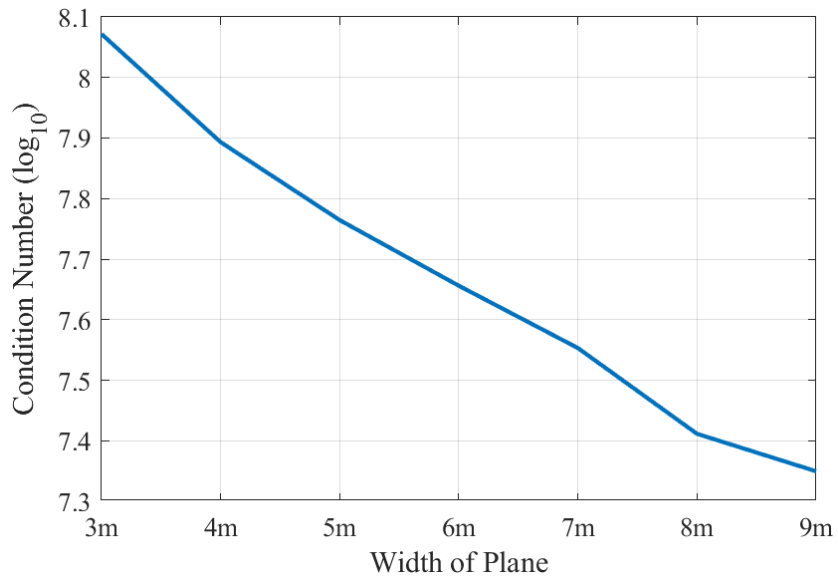
#### 4.2.2. Width of Plane

Calibration S-II was successively conducted by increasing the plane widths by 1m to analyze the impact of the dimensions of incorporated planes. Increasing the dimension of the plane provides a variety of horizontal angle and range observations.

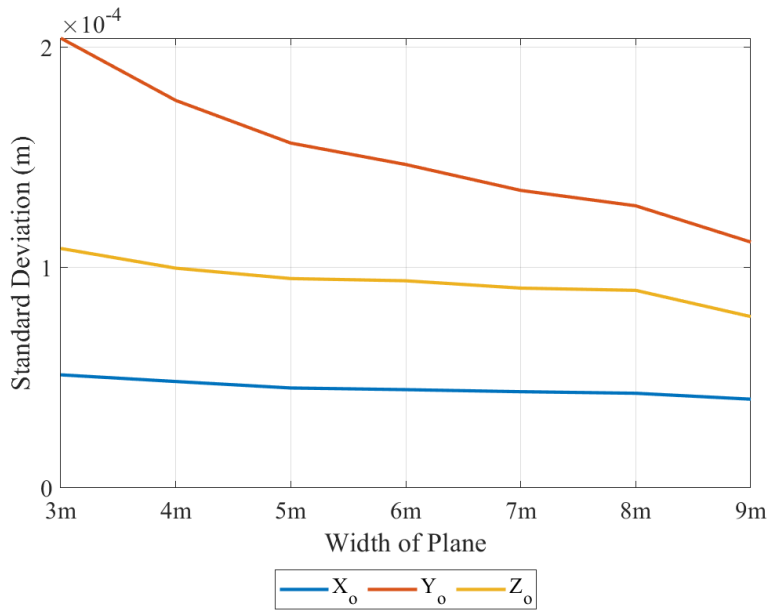
As shown in Table 4-5, MAE of AP values were all reasonably small and consistent. Therefore, precision of estimated calibration parameters was investigated for the analysis in Calibration S-II. As can be seen in Figure 4-3(a), linear dependence was reduced by increasing the dimension of the incorporated planes. The averaged standard deviations of the estimated parameters are shown in Figure 4-3(b) to (f). Results showed clear tendency of decreasing standard deviation except vertical angular offset. This indicates that vertical angular offsets are not correlated with the width of planes. However, the standard deviation of the vertical angular offset eventually dropped off as the precision of other parameters increases. From these observations, utilizing a large planar feature enables the estimation of more accurate parameters in general.

**Table 4-4.** RMSE of AP Values in Calibration S-II

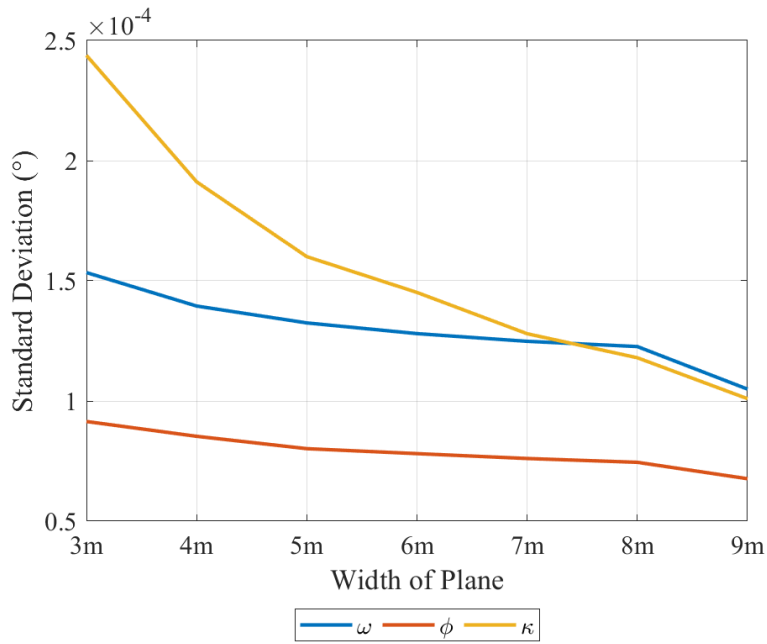
<b>Plane Width</b>	<b><i>D</i> (m)</b>	<b><math>\Delta\theta</math> (deg)</b>	<b><math>\Delta\alpha</math> (deg)</b>
3 m x 5m	0.006	0.003	0.005
4 m x 5m	0.006	0.003	0.005
5 m x 5m	0.005	0.003	0.004
6 m x 5m	0.006	0.002	0.004
7 m x 5m	0.005	0.002	0.004
8 m x 5m	0.005	0.001	0.004
9 m x 5m	0.005	0.003	0.005



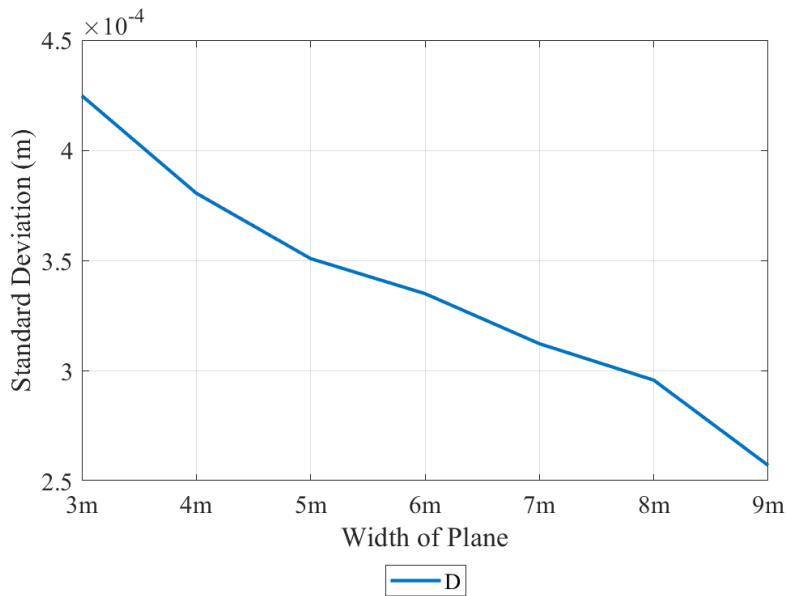
(a) Condition Number of Design Matrix



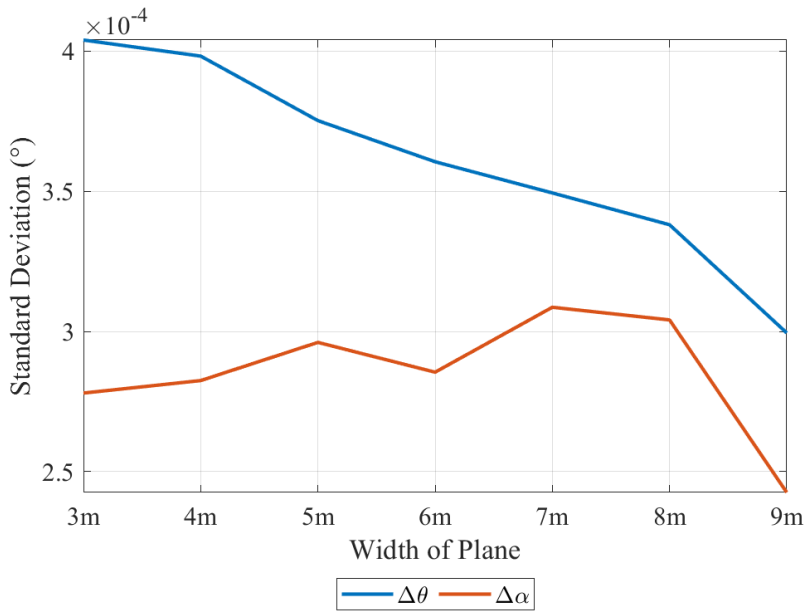
(b) Precision of Estimated Scanner Position Parameters



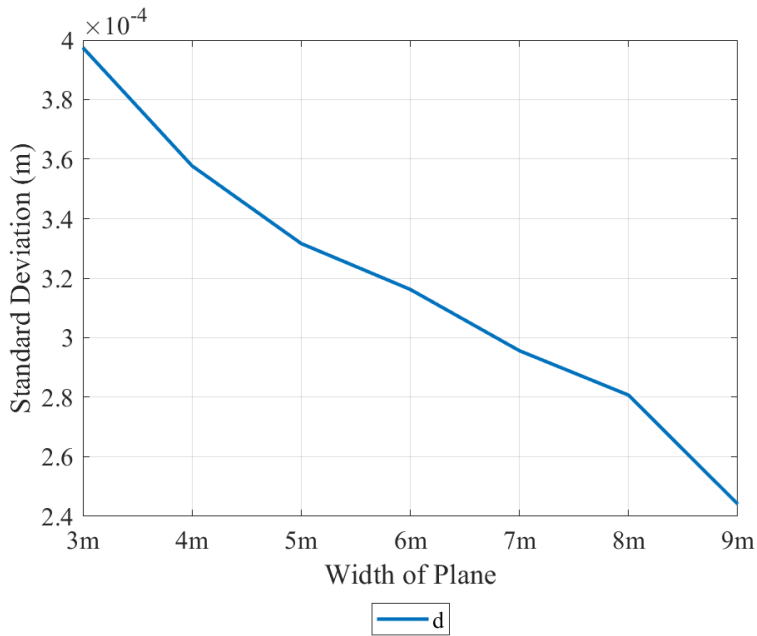
(c) Precision of Estimated Scanner Rotation Angle Parameters



(d) Precision of Distance Offset



(e) Precision of Angular Offsets



(f) Precision of Plane Parameter ( $d$ )

**Figure 4-3. Calibration Results of Calibration S-II**

### 4.2.3. Number of Incorporated Planes

Calibration S-III was conducted to analyze the impact of including various planar features. As shown in Figure 4-4, as more planes were incorporated into the adjustment, more planes were placed and surrounded around the scanner's location. Table 4-6 shows the RMSE of AP values. RMSE decreased continuously as more planes were used. Figure 4-5(a) also clearly shows the decrease of linear dependence. It is noteworthy that distance offset and plane parameter ( $d$ ) are adversarial each other. As more planes are used, the geometrical feature of acquired point cloud data changes from planes to circle. Then, distance offset and plane parameter  $d$  acts similar in terms of pushing or pulling the point cloud.

When compared with tests in similar situations involving five planes (Calibration S-II), calibration results can be obtained more accurately than the case of including five planes in Calibration S-III. Consequently, the inclusion of "surrounding" planes is more significant in comparison to the increase of incorporated planes.

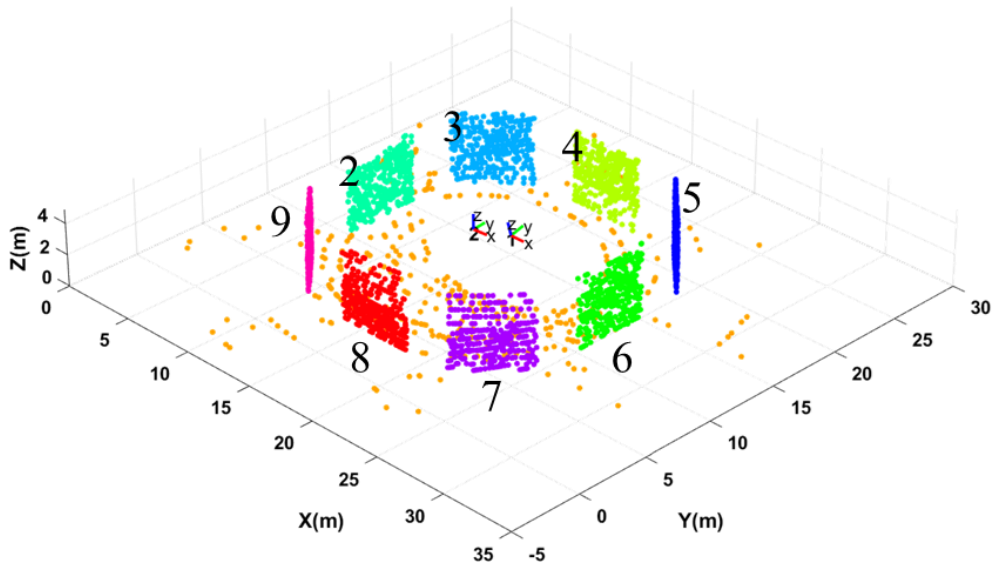
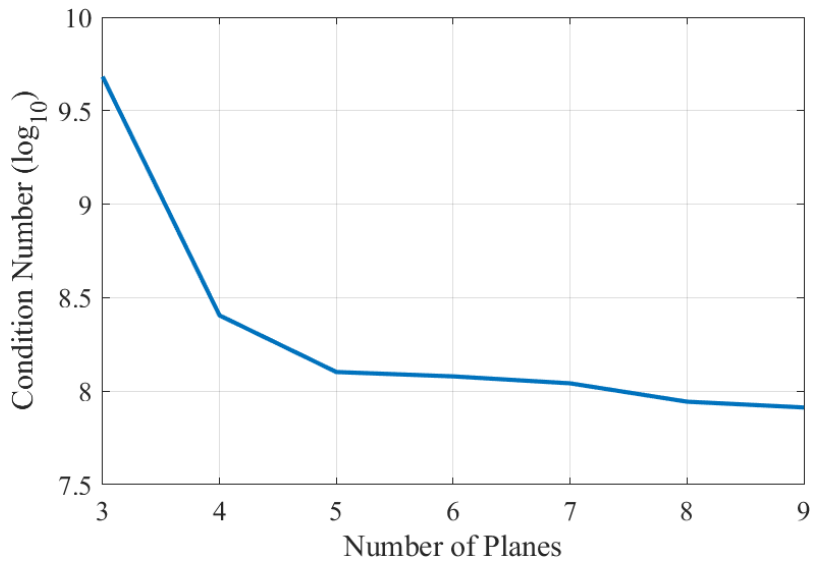


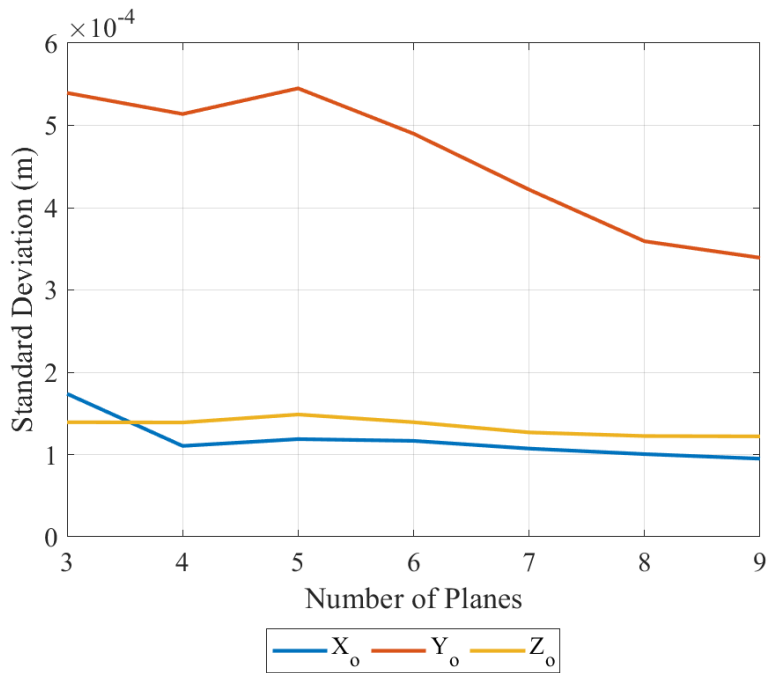
**Figure 4-4.** Overview of Calibration S-III (Labeled number indicates used planes in calibration)

**Table 4-5.** RMSE of AP Values in Calibration S-III

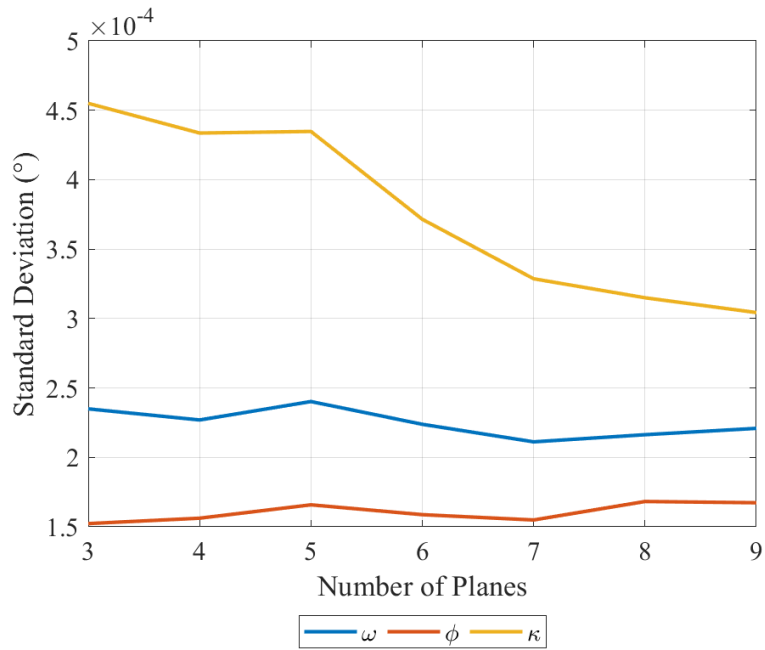
Used Planes	$D$ (m)	$\Delta\theta$ (deg)	$\Delta\alpha$ (deg)
1 - 3	0.010	0.040	10.941
1 - 4	0.013	0.007	0.104
1 - 5	0.014	0.007	0.035
1 - 6	0.013	0.004	0.033
1 - 7	0.013	0.006	0.031
1 - 8	0.014	0.006	0.030
1 - 9	0.014	0.003	0.030



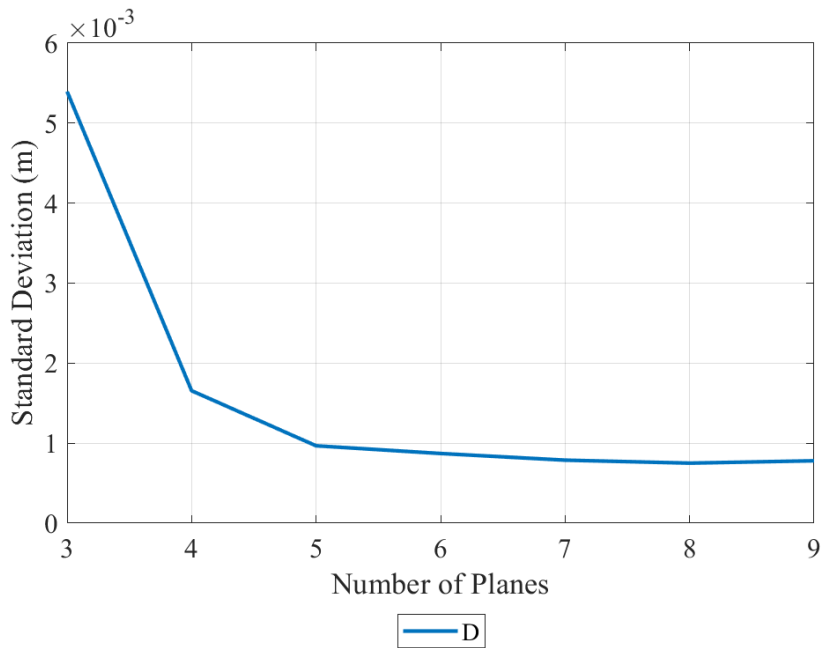
(a) Condition Number of Design Matrix



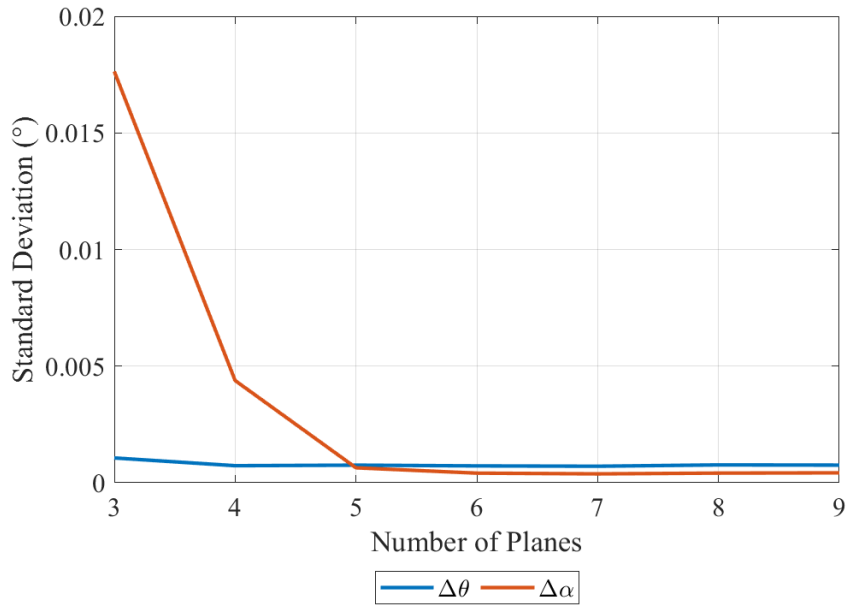
(b) Precision of Estimated Scanner Position Parameters



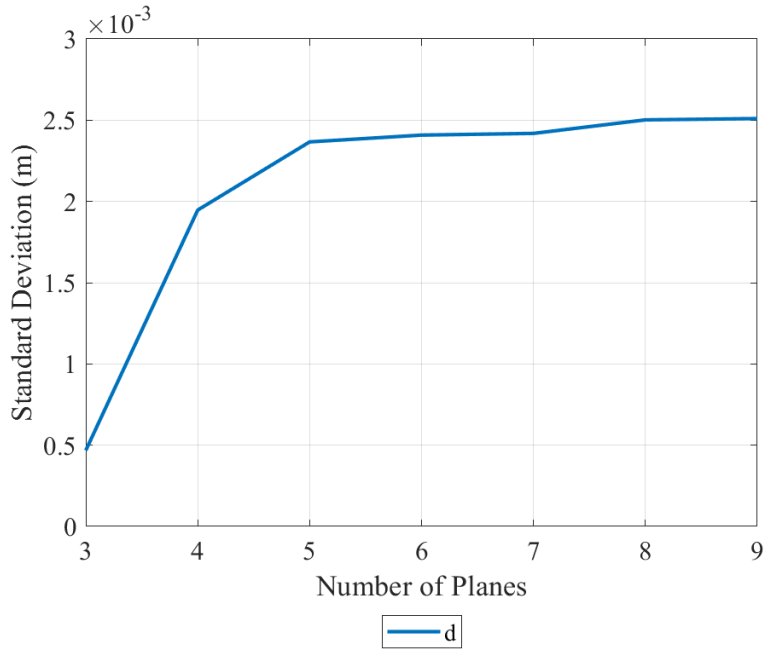
(c) Precision of Estimated Scanner Rotation Angle Parameters



(d) RMSE of Distance Offset



(e) RMSE of Angular Offsets



(f) RMSE of Plane Parameter ( $d$ )

**Figure 4-5.** Calibration Results of Calibration S-III

#### 4.2.4. Network Geometry

Calibration S-IV was performed to analyze the impact of network geometry. Figure 4-6 shows the five cases for different network geometry. As the second epoch moves toward the corner of the planes, a wider variety of range observation can be acquired than when scanning from the center (as seen by the location of Case 1). Figure 4-6(a) illustrates the linear dependency decrease as the second epoch moves toward the corner of the test sites. RMSE of distance offset, vertical angular offset and plane parameter ( $d$ ) decreased as well as MAE of scanner orientation angle ( $\omega$ ) as the second epoch approached to the corner. This indicates that using scan data that is captured at the corner can be helpful to perform accurate *in situ* calibration. Whenever facing the corner during data acquisition, one can tilt the sensor system slightly at the corner to set the reference epoch for frequent *in situ* calibration.

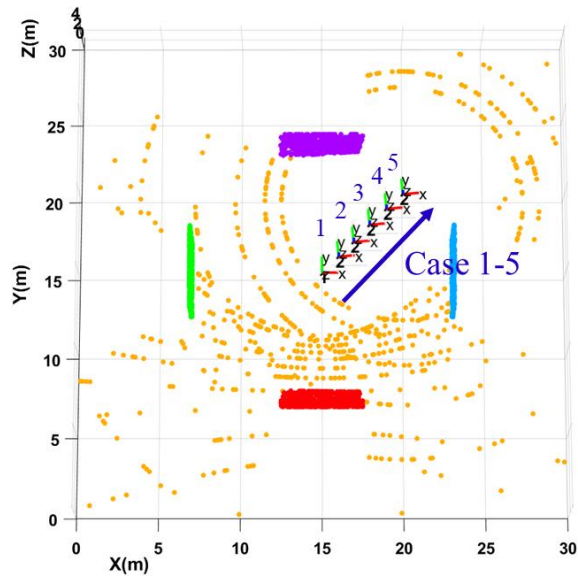
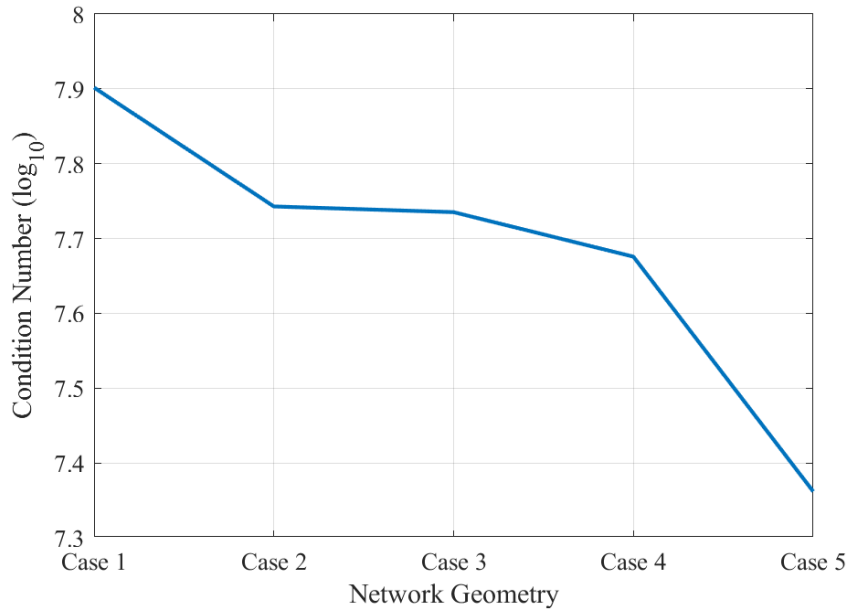


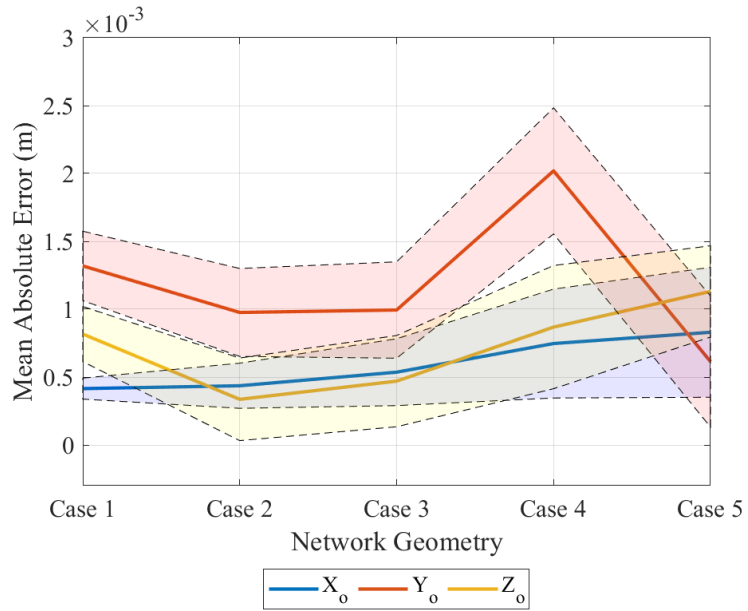
**Figure 4-6.** Overview of Calibration S-IV

**Table 4-6.** RMSE of AP Values in Calibration S-IV

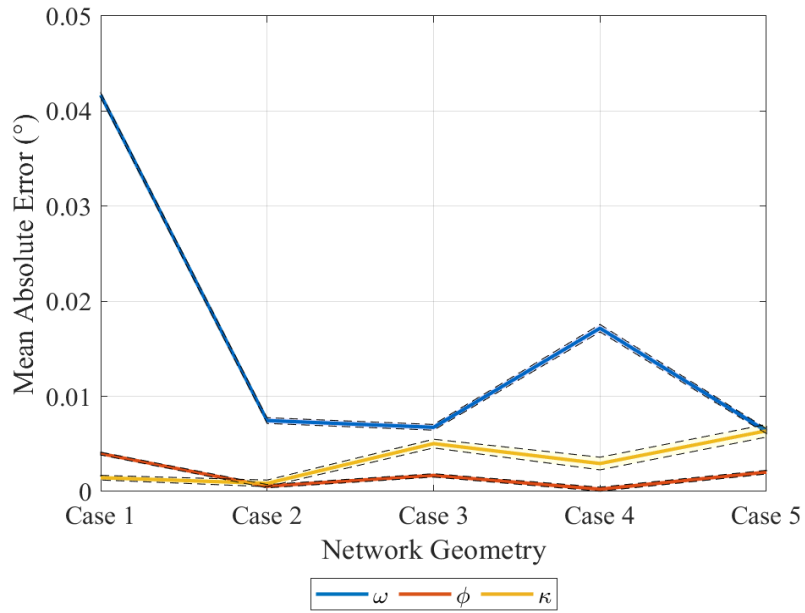
<b>Cases</b>	<b><math>D</math> (m)</b>	<b><math>\Delta\theta</math> (deg)</b>	<b><math>\Delta\alpha</math> (deg)</b>
1	0.015	0.003	0.031
2	0.006	0.003	0.014
3	0.006	0.003	0.011
4	0.006	0.004	0.020
5	0.006	0.003	0.008



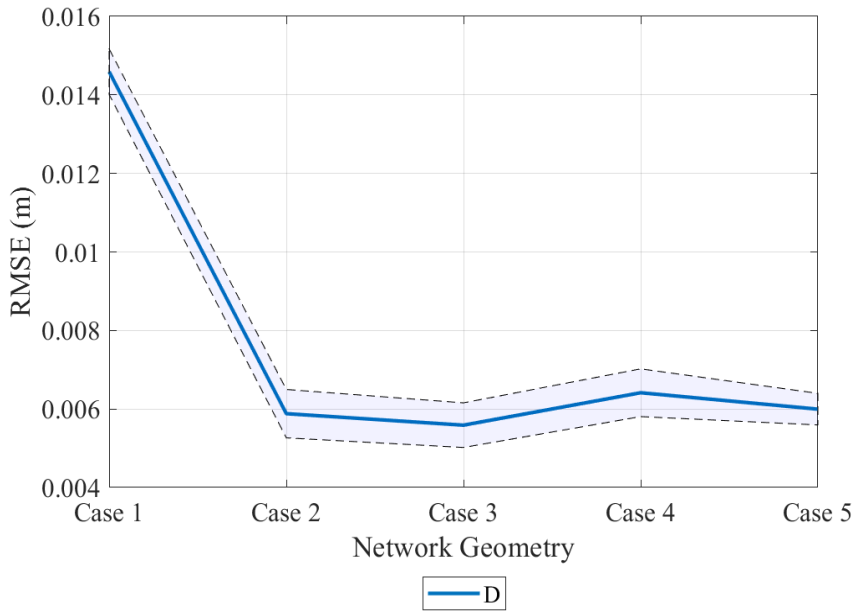
(a) Condition Number of Design Matrix



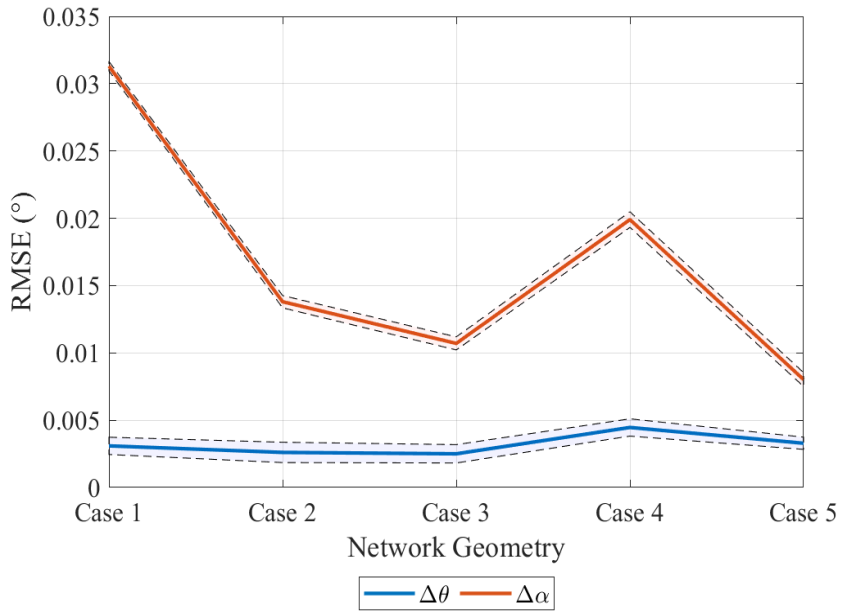
(b) MAE of Scanner Position Parameters



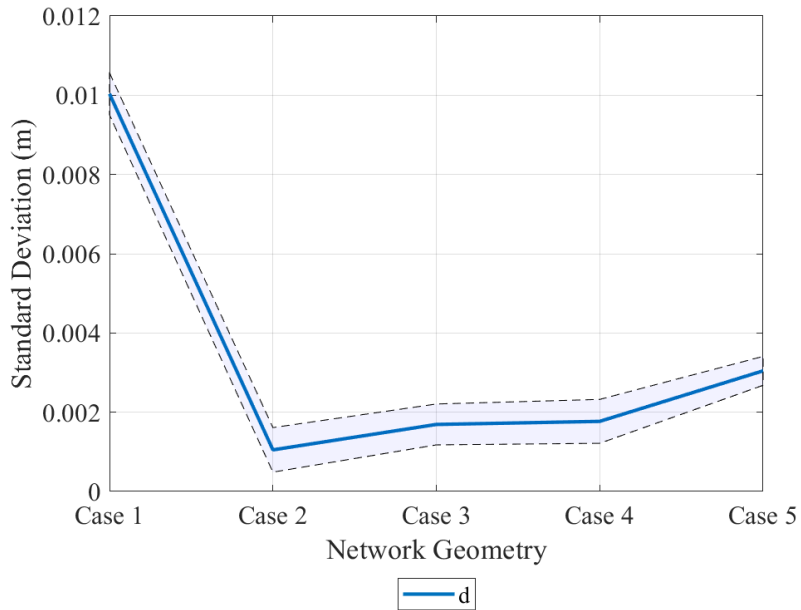
(c) MAE of Scanner Orientation Parameters



(d) RMSE of Distance Offset



(e) RMSE of Angular Offsets



(f) Distance between Scanner and Planes

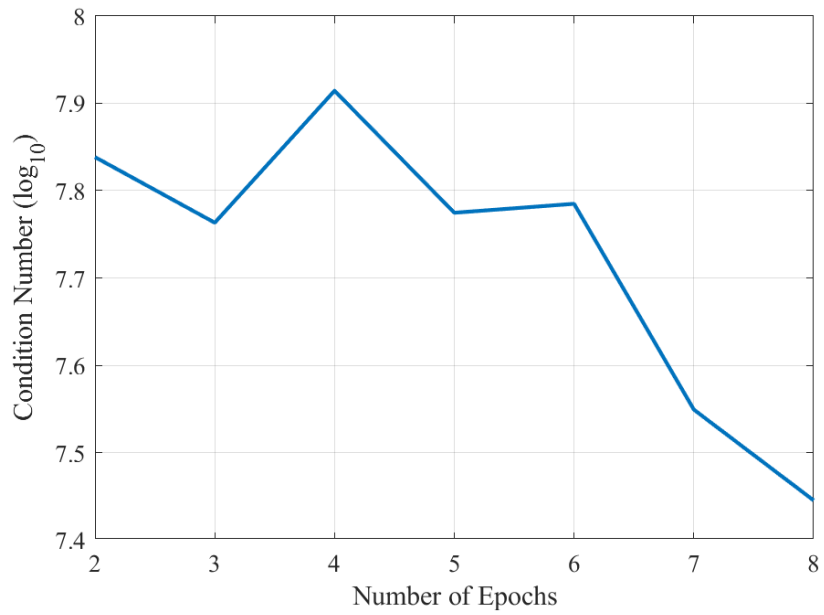
**Figure 4-7.** Calibration Results of Calibration S-IV

#### 4.2.5. Number of Incorporated Epochs

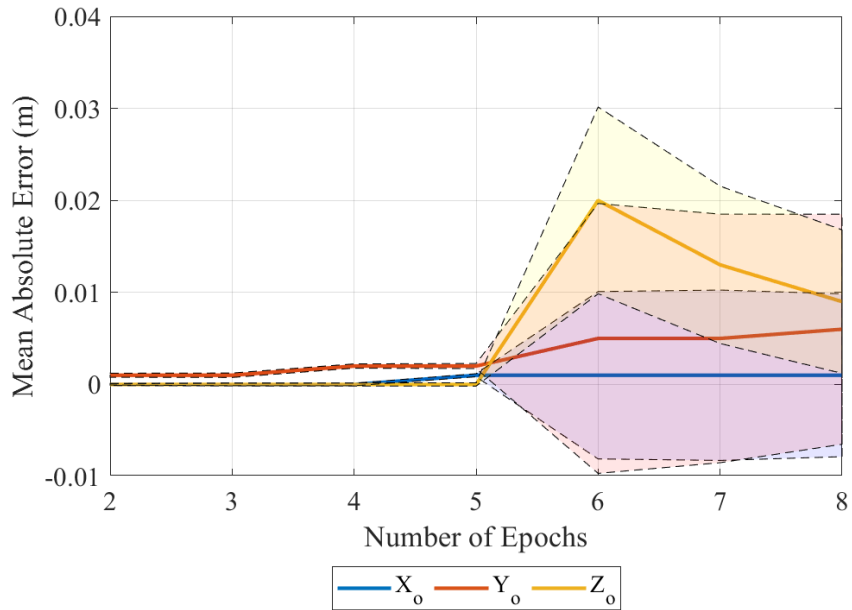
Calibration S-V was performed to analyze the impact of incorporating multiple epochs in the adjustment. RMSE of AP values in Calibration S-V is shown in Table 4-7. RMSE of AP values were significantly increased when more than five epochs of epochs were incorporated. Figure 4-8(a) demonstrates that incorporating a large number of epochs reduces the condition number of normal equations; however, MAE and RMSE of estimated calibration parameters increased drastically when the number of incorporated epochs exceeded five, which is the number of incorporated planes in the adjustment. It is reasonable that assume that the objective function is more effectively adjusted by plane parameters than the locations and orientations of the scanners if the number of epochs exceeds the number of incorporated planes. This indicates that using multiple epochs in the adjustment can reduce linear dependence of design matrix but can significantly reduce the accuracy of calibration results if too many epochs are used in the adjustment. Therefore, the number of common planes needs to be specified before incorporating multiple epochs.

**Table 4-7.** RMSE of AP Values in Calibration S-V

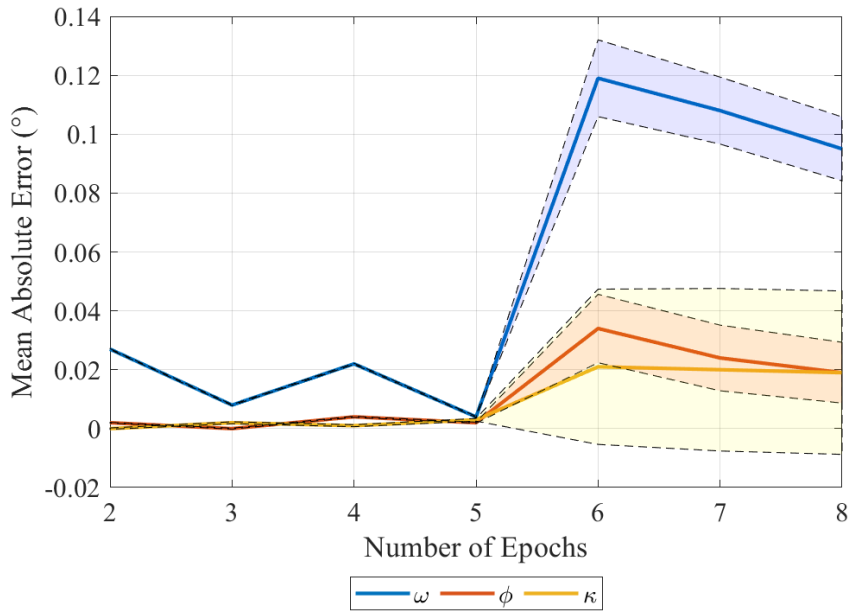
<b>No. of Epochs</b>	<b><math>D</math> (m)</b>	<b><math>\Delta\theta</math> (deg)</b>	<b><math>\Delta\alpha</math> (deg)</b>
2	0.013	0.002	0.026
3	0.007	0.003	0.017
4	0.010	0.002	0.031
5	0.006	0.003	0.032
6	0.072	0.021	0.069
7	0.048	0.053	0.055
8	0.033	0.079	0.045



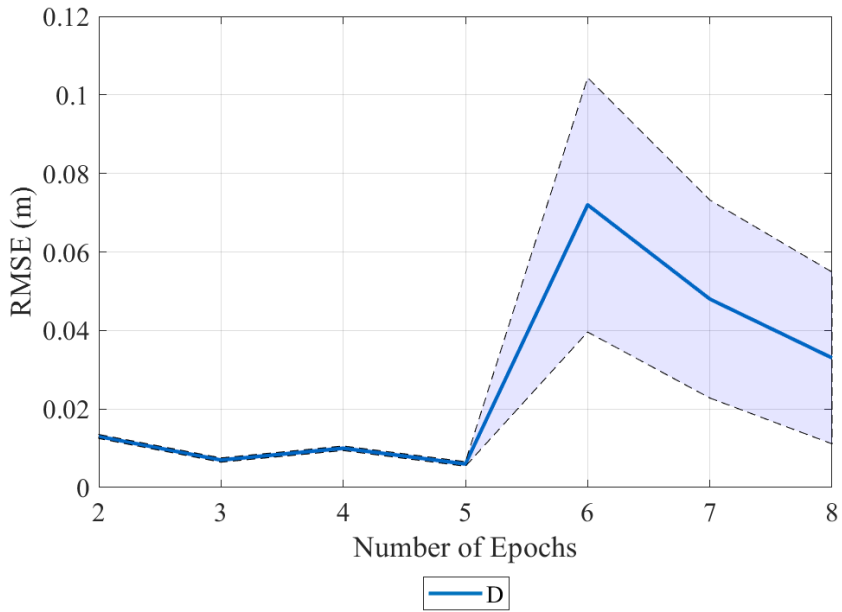
(a) Condition Number of Design Matrix



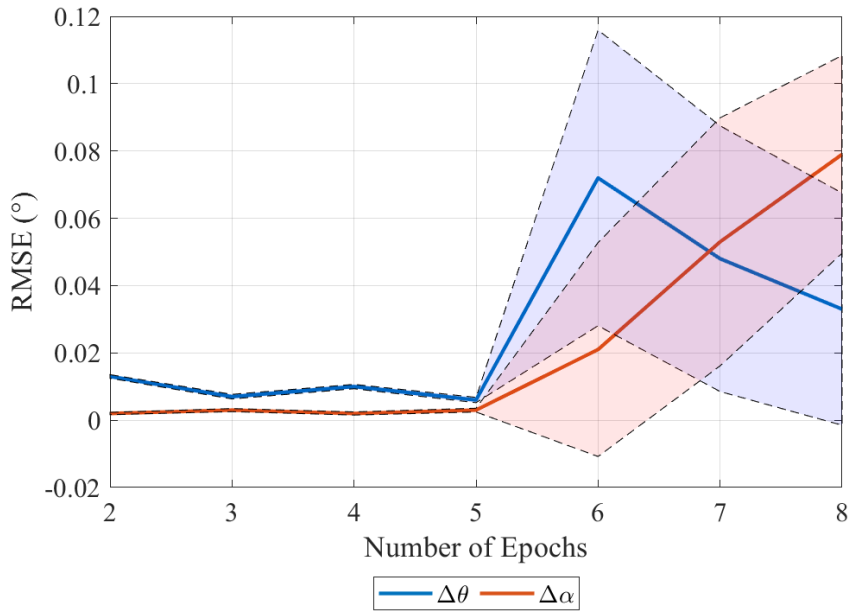
(b) MAE of Scanner Position Parameters



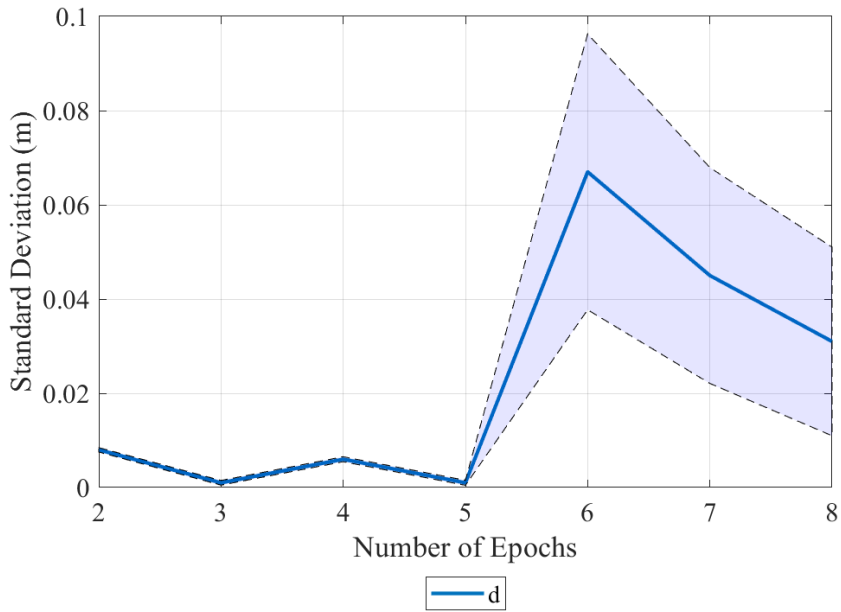
(c) MAE of Scanner Orientation Parameters



(d) RMSE of Distance Offset



(e) RMSE of Angular Offsets



(f) RMSE of Plane Parameter ( $d$ )

**Figure 4-8.** Calibration Results of Calibration S-V

### 4.3. Summary of the Section

In order to establish a calibration dataset for accurate plane-based self-calibration, experiments were conducted using simulated datasets with specific conditions including tilted angle, dimension of incorporated planes, number of planar features, network geometry, and number of incorporated epochs. First, selecting a reference epoch that defines PPs is crucial because it provides the planar constraints for all point cloud data to be fit into. The reference epoch should be slightly tilted to avoid linear dependence in the design matrix. Second, the width of the planar features should not be narrow because narrow planes have a lower variety of range and horizontal angle observations, thus decreasing the total accuracy of the adjustment. Third, at least three planes, one horizontal plane and two vertical planes that are not parallel to each other, must be incorporated to estimate scan locations. Using a large number of planes can increase the accuracy of the adjustment, but the geometry of the planes should be “surrounding” the scan locations in order to obtain more accurate self-calibration results. Fourth, the sensor location near the corner of the planes can provide a variety of range observations which can be helpful to accurately estimate APs. Lastly, the number of incorporated epochs must not exceed the number of incorporated planes.

## 5. Proposed Self-Calibration Framework

### 5.1. Self-Calibration Framework

To perform accurate self-calibration, estimating the functional model of the reference target is essential. If the plane functional model and EOPs are estimated accurately, APs can be estimated accurately as well. Previous researches revealed that a scale factor varied with a magnitude of 0.001, which affects an error of 1cm at 10m range (Lichti *et al.*, 2010; Chan *et al.*, 2015). Considering VLP-16 has a range accuracy of up to 3 cm, the systematic errors caused by the scale factor can be considered as noise for up to the 30m range. With this assumption, plane parameters and sensor EOPs can be estimated without compromising the overall accuracy of estimated parameters even if a linear scale factor is not considered.

Based on the conditions set for the simulated dataset experiments in Section 4, this research proposes a self-calibration framework which can be described by the following process. First, acquire point cloud with a tilted angle at the corner of the indoor environment. Then, extract the planes which fit around noise level and count the number of extracted planes. Next, using successive epochs, add multiple scan data that does not

exceed the number of extracted planes to the calibration dataset. Then, planes within each scan data are extracted and matched. With these plane-matched point clouds, EOPs for each epoch, PPs for each plane, and APs excluding scale factor for each laser are estimated simultaneously. Subsequently, if RMSE converges, the estimated EOP and PP are fixed, and APs are initialized. Lastly, estimate all APs simultaneously using the fixed EOP and PP. The flow chart of the proposed self-calibration framework is illustrated in Figure 5-1.

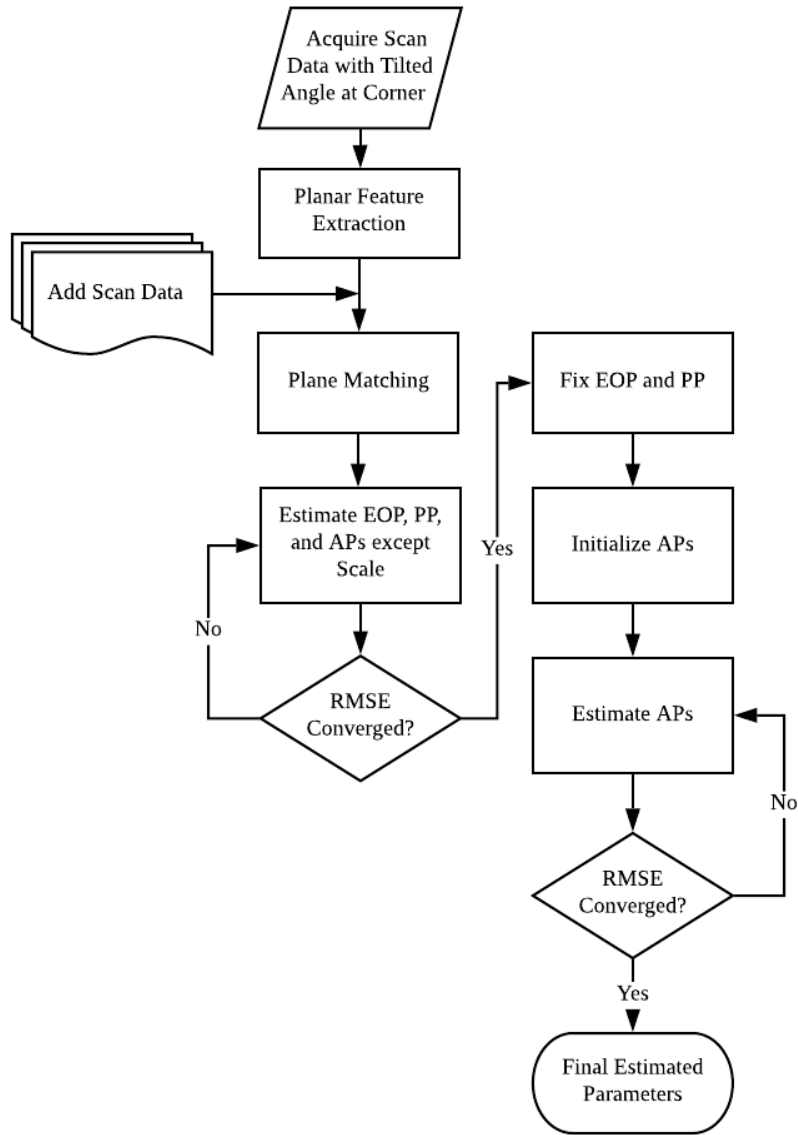


**Figure 5-1.** Flow chart of Proposed Self-Calibration Framework

## 5.2. Experiment Description

### 5.2.1. Simulated Datasets

In this section, the proposed self-calibration framework will be performed using a simulated dataset. The data acquisition environment was built via simulation, representing a reasonable indoor environment (Figure 5-2). The magnitude of the AP was set to the same values as that of Table 4-1, while the random noises were added by 1 cm, 0.025 degree, and 0.01 degree for range, horizontal angle observation, and fixed vertical angle, respectively. The generated point cloud is shown in Figure 5-3 and the detected planes for the dataset are given in Figure 5-4. As shown in Figure 5-2, the reference epoch was tilted by approximately  $-30^\circ$  near the corner of the indoor environment. A total of six vertical planes and one horizontal plane was extracted from the reference epoch. The summary of the calibration dataset is given in Table 5-1.

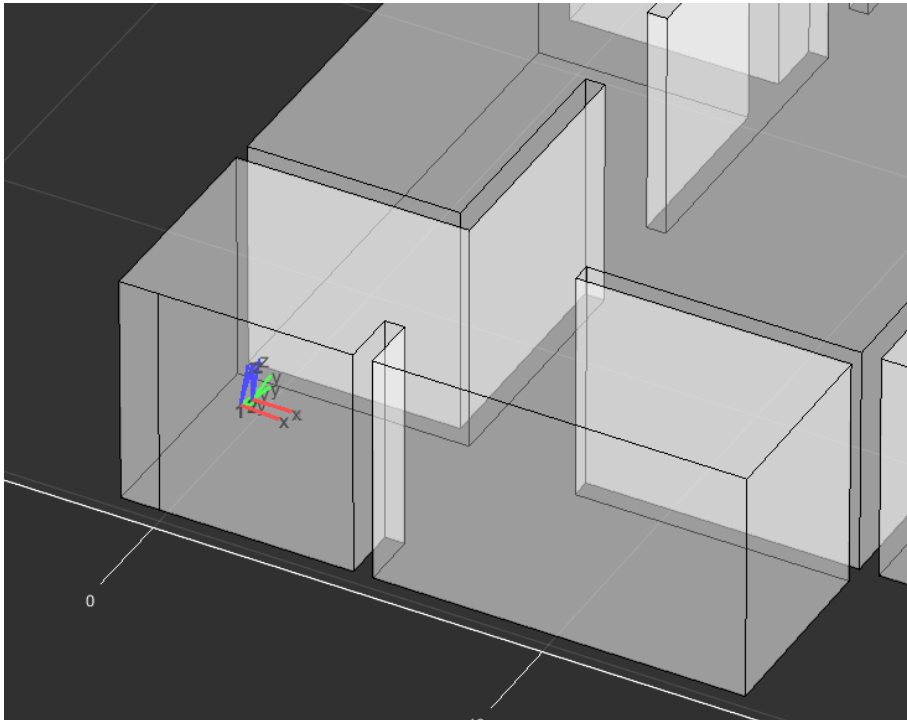
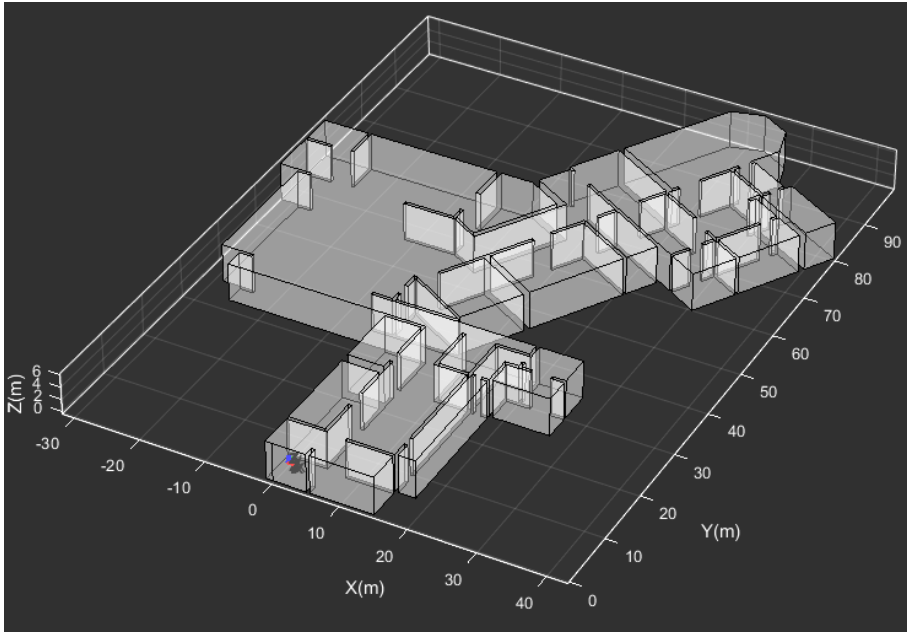


**Figure 5-2.** Simulated Indoor Environment and Scan Locations

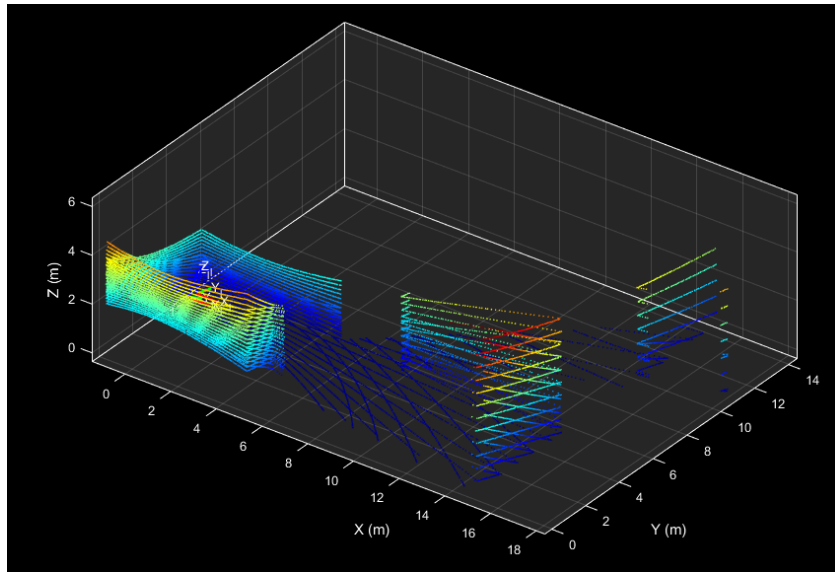


**Figure 5-3.** Generated Point Cloud

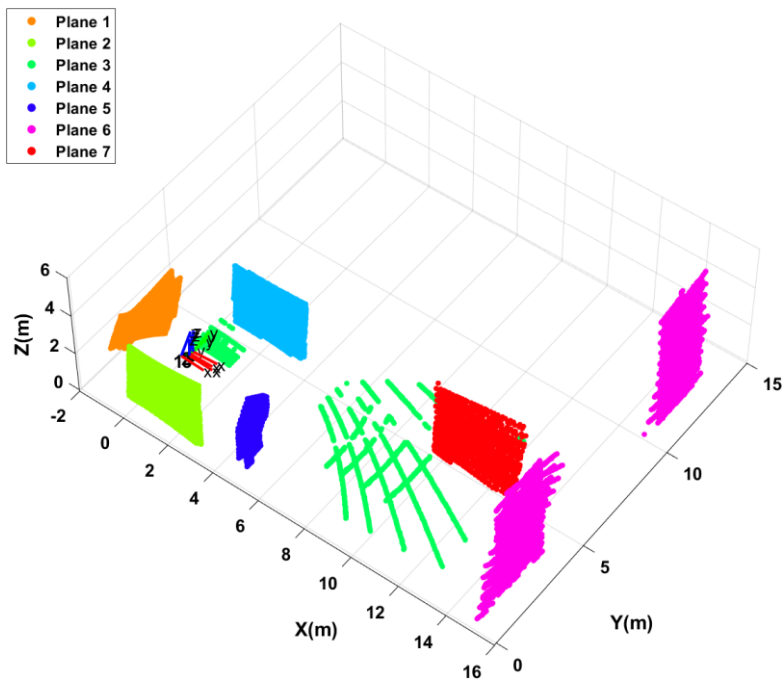


**Figure 5-4.** Calibration Dataset and Matched Planes

### 5.2.2. Real Dataset

A real dataset was captured using a backpack platform sensor system as shown in Figure 5-5. The sensor system consisted of two VLP-16 and three fish-eye lens cameras with a GNSS/INS system. The point cloud was acquired in an indoor environment where the planar features can be easily detected. The data acquisition site was selected to be in a corridor with an approximate dimension of 2.5 m x 40 m x 2.5 m, which included four major vertical planes and two horizontal planes, as demonstrated in Figure 5-6. The summary of the calibration dataset is shown in Table 5-1 and the captured point cloud is depicted in Figure 5-7.

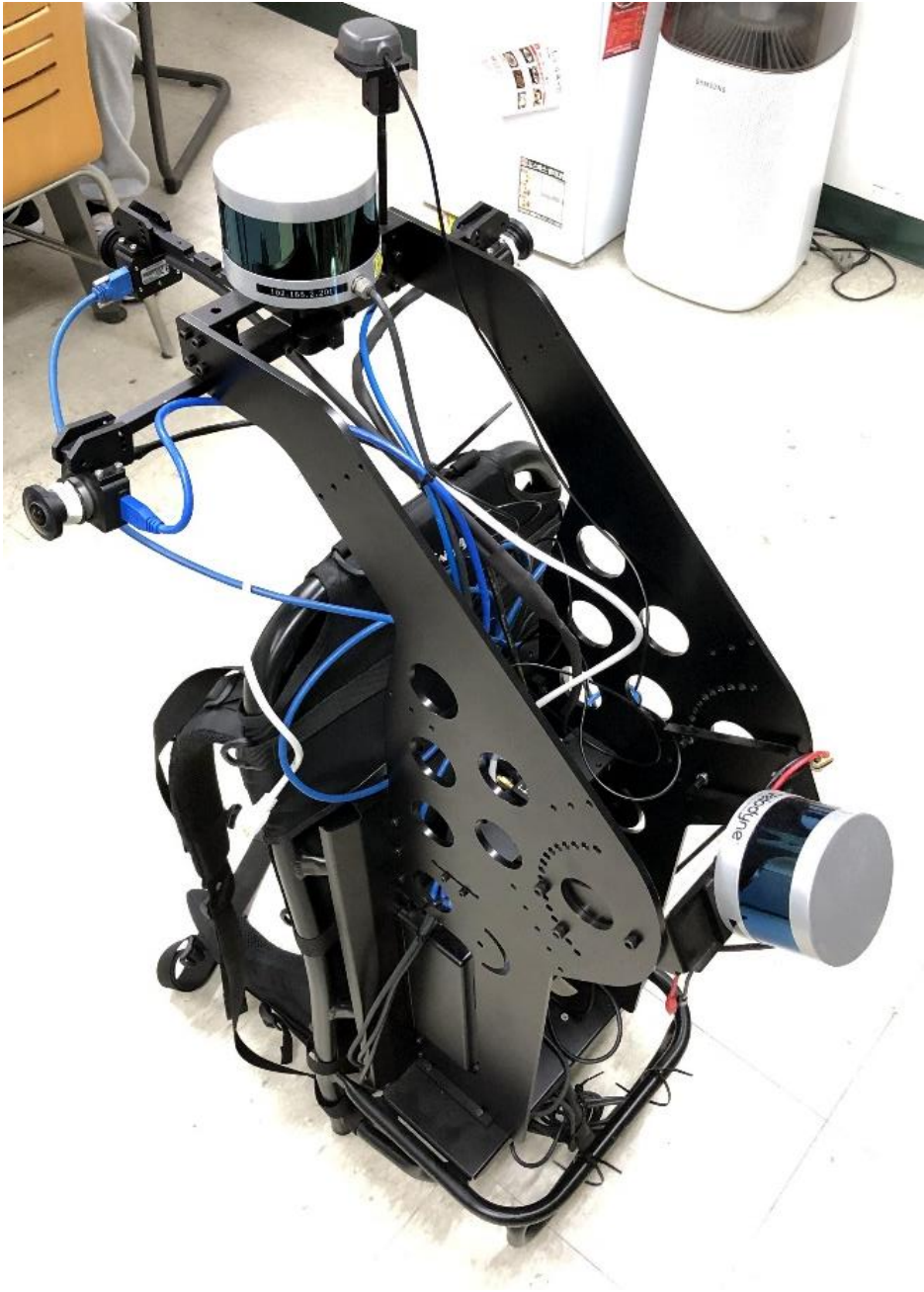


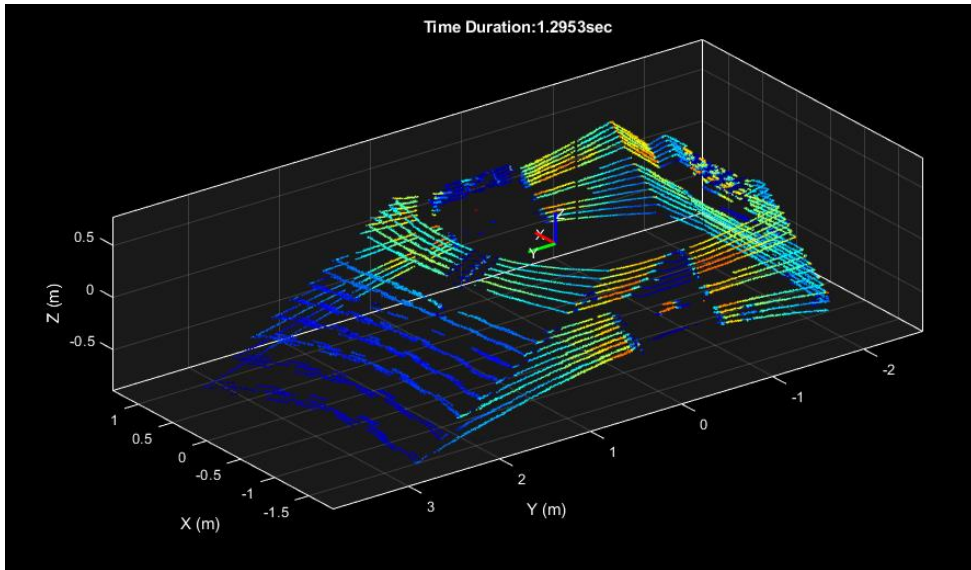
**Figure 5-5.** Backpack Platform Sensor System



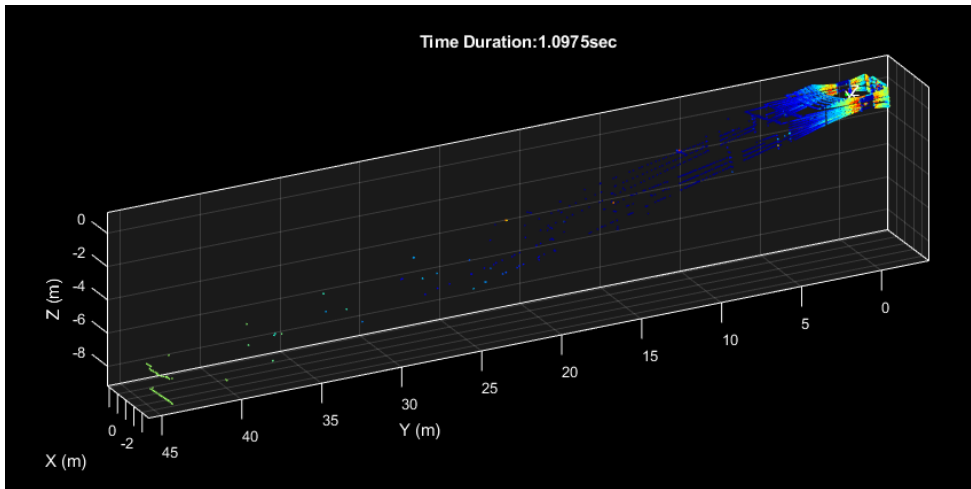
**Figure 5-6.** Acquisition Site of the Real Dataset

**Table 5-1.** Summary of Calibration Using the Real Dataset

<b>Calibration</b>	<b>Sweep</b>	<b>No. of Points</b>	<b>No. of Planes</b>	<b>Tilted Angle</b>	<b>Variiances</b>
R-I	1	56,215	7	20°	Range: 0.01m /
	2	26,485	7	0°	Angle: 0.025°



(a) Epoch 1



(b) Epoch 2

**Figure 5-7.** Point Cloud of Real Dataset Captured at Two Epochs

## 6. Results and Analysis

### 6.1. Calibration Results with Simulated Datasets

The accuracy of the proposed self-calibration framework was evaluated by examining planar misclosure, measurement residuals, deviations of estimated parameters, correlations between parameters, and visual analysis. A plot showing planar misclosure before and after adjustment is given in Figure 6-1 with the associated statistics provided in Table 6-1. Results showed approximately 98% in improvement of planar misclosure. Note that only the APs changed, and other parameters were fixed to consider only the result of self-calibration.

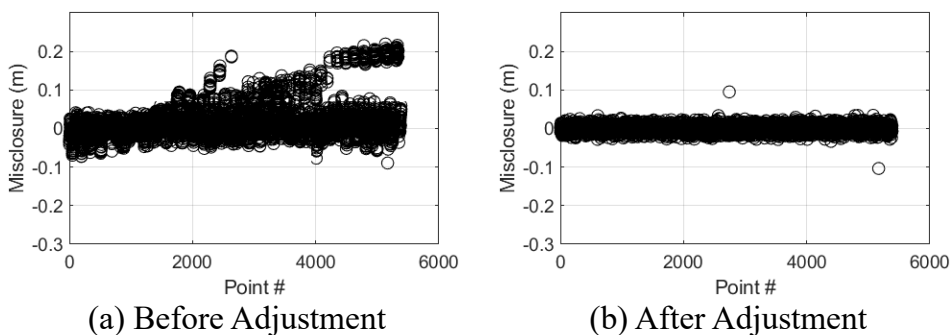


**Figure 6-1.** Planar Misclosure of Proposed Self-Calibration Approach

**Table 6-1.** Statistics of Planar Misclosure of Proposed Self-Calibration Approach

<b>(m)</b>	<b>Min</b>	<b>Max</b>	<b>Mean</b>	<b>RMSE</b>
Before	-0.0894	0.2193	0.0184	0.0508
After	-0.1035	0.0950	0.0000	0.0085

In Table 6-2, the mean absolute difference between estimated and preset AP values are provided. Given the preset AP values (Table 4-1), all AP values were reasonably estimated, thereby reducing the difference between preset values. In the proposed self-calibration framework, the scale factor was also estimated along with the other parameters.

**Table 6-2.** Mean Absolute Difference between Estimated Parameters and Preset Values of Calibration SP-I

<b><math>S</math></b>	<b><math>D</math> (m)</b>	<b><math>\Delta\theta</math> (deg)</b>	<b><math>\Delta\alpha</math> (deg)</b>
0.0002	0.0025	0.0219	0.0093

Measurement residuals were also examined. Figure 6-2 shows the range and horizontal angle observation residuals. As shown in Figure 6-3, range residuals display a nearly normal distribution plot, which signifies that the adjustment estimated the calibration parameters accurately. However, in the case of the horizontal angle residuals, systematic error can

be seen to linger even after the adjustment. This result indicated that the linear scale factor was not estimated accurately enough in the adjustment. To solve this problem, specifying a highly accurate reference target location and the sensor's location for parameter decorrelation are essential.

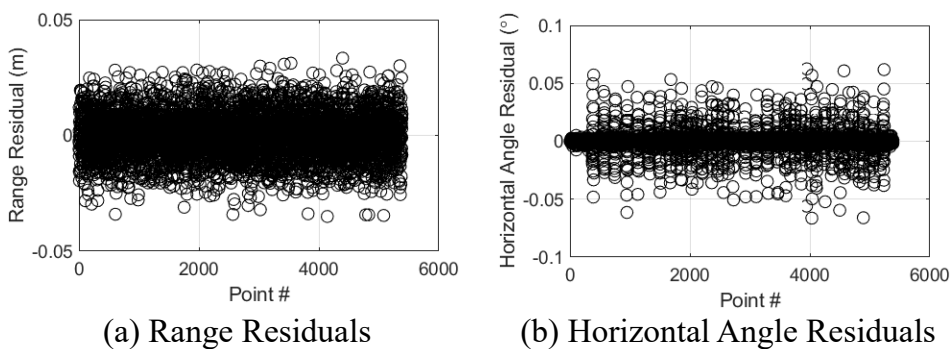


**Figure 6-2.** Measurement Residuals and Range RMSE

In addition, the correlation matrix can be analyzed to investigate the accuracy of the adjustment. The averaged correlation coefficients are given in Table 6-3. Overall, correlations between parameters showed low values, except for the correlation between the linear scale factor and the distance offset. These two parameters have the same effect of pushing or pulling the plane, inevitably resulting in high correlation coefficients. As discussed in Section 3.2.1, since only a variety of range observation can decorrelate these parameters, a long baseline between the sensor locations is required.

**Table 6-3.** Averaged Correlation Coefficients Between Estimated Parameters of Calibration SP-I

	$X_o$	$Y_o$	$Z_o$	$\omega$	$\phi$	$\kappa$	$S$	$D$	$\Delta\theta$	$\Delta\alpha$
$X_o$	-	0.231	0.237	0.146	0.125	0.229	-	0.047	0.314	0.338
$Y_o$		-	0.530	0.325	0.078	0.138	-	0.168	0.493	0.536
$Z_o$			-	0.330	0.062	0.112	-	0.144	0.592	0.446
$\omega$				-	0.074	0.202	-	0.198	0.142	0.220
$\phi$					-	0.593	-	0.127	0.162	0.032
$\kappa$						-	-	0.082	0.274	0.077
$S$							-	0.824	0.178	0.274
$D$								-	0.204	0.268
$\Delta\theta$									-	0.426
$\Delta\alpha$										-

Figure 6-3 illustrates all point clouds acquired before and after the adjustment to perform visual analysis of the calibration results for further evaluation. In Figure 6-4, the deviation of the plane at region 1 and 2 decreased as well as the translation and rotation distortions were corrected.

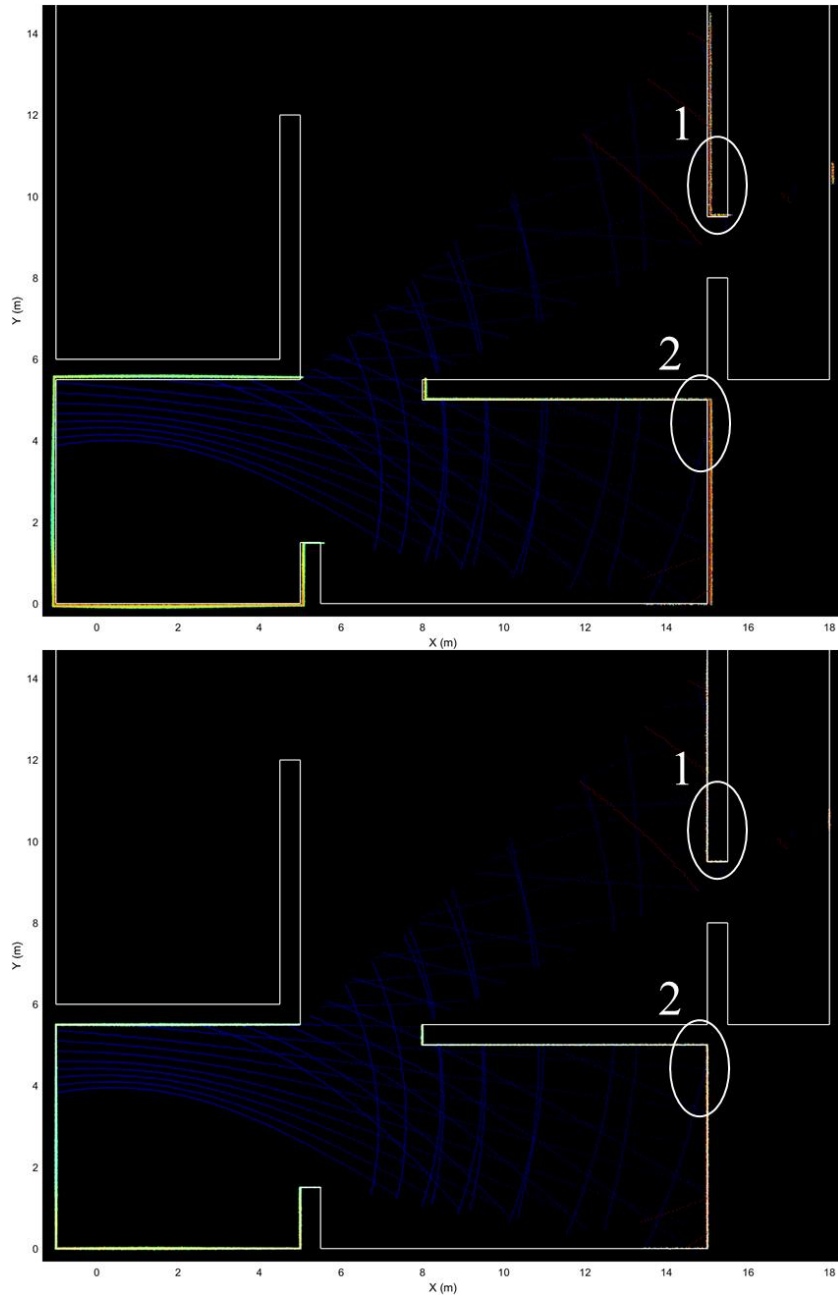
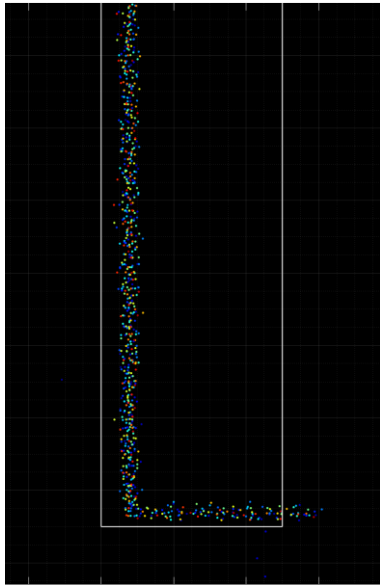
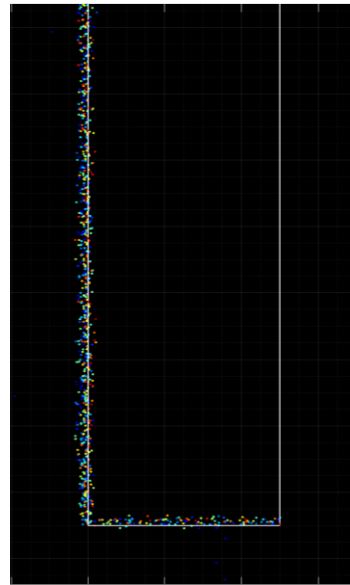


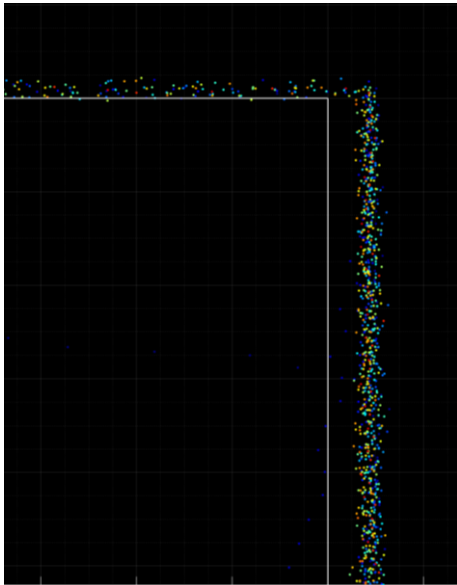
**Figure 6-3.** Top View of Point Cloud Before (Upper) and After (Lower) Adjustment



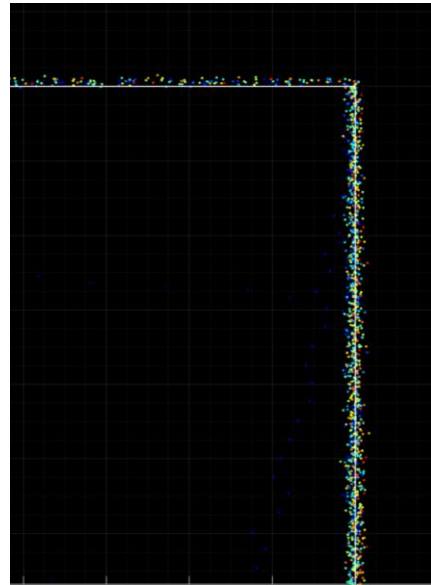
(a) Before Adjustment - 1



(b) After Adjustment - 1



(c) Before Adjustment - 2



(d) After Adjustment - 2

**Figure 6-4.** Close-up of the Calibration Result (True planes are represented by white lines)

Also, estimated planes from before and after the adjustment are shown in Figure 6-5. Estimated planes after the adjustment fit well into the ideal planes, while estimated planes before the adjustment showed rotations and translations.

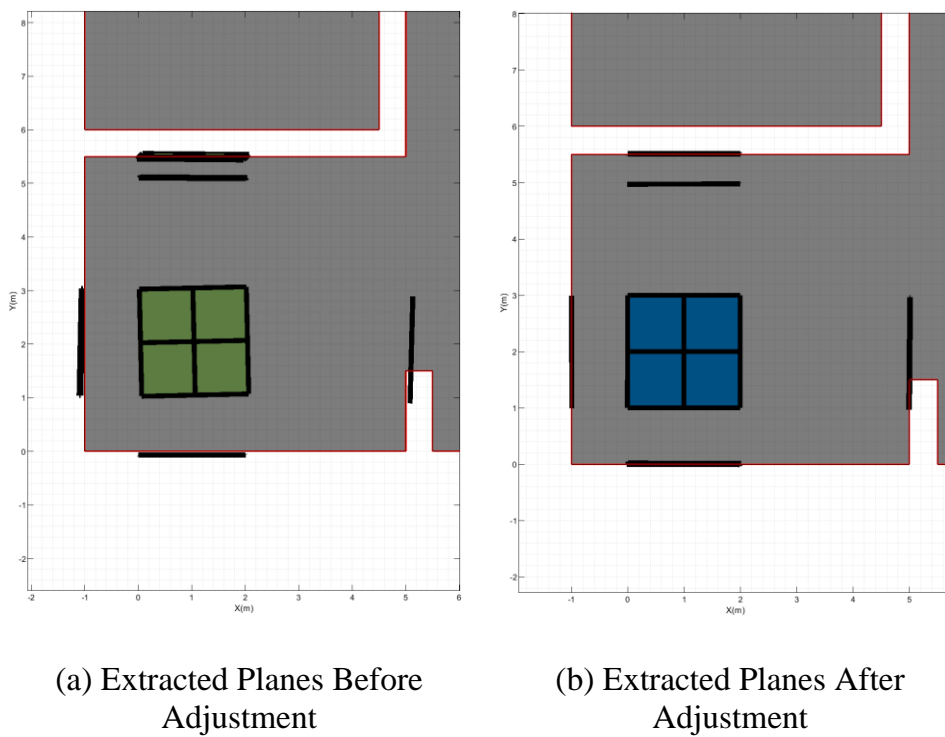


**Figure 6-5.** Estimated Planes Before and After Adjustment

## 6.2. Calibration Results with Real Dataset

Calibration using a real dataset was performed and the accuracy was analyzed by examining planar misclosure before and after adjustment, range and horizontal angle observation residuals, correlations, and the accuracy of estimated parameters.

Table 6-3 shows the summary of the results regarding planar misclosure. For planar misclosure calculations, miscellaneous parameters such as EOPs and plane parameters were held to the same value in order to compare the results from self-calibration. The calibration result showed an improvement of planar misclosure RMSE by 49% after the adjustment. The planar misclosure results before and after adjustment is given in Figure 6-6.

**Table 6-4.** Summary of Planar Misclosure

<b>(m)</b>	<b>Min</b>	<b>Max</b>	<b>Mean</b>	<b>RMSE</b>
Before	-0.0684	0.0702	-0.0013	0.0196
After	-0.0886	0.0577	-0.0001	0.0083

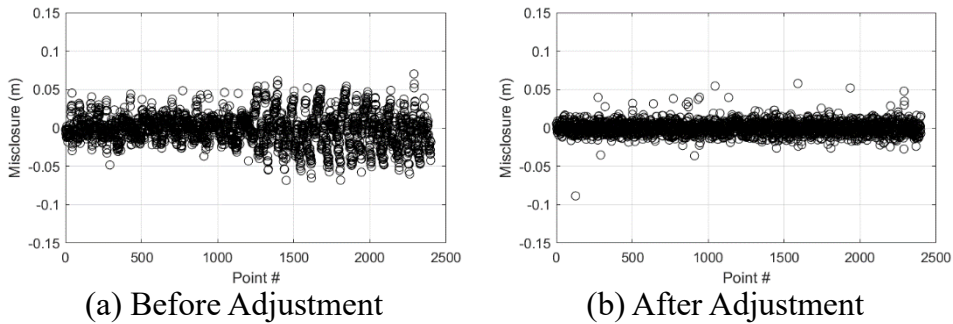


**Figure 6-6. Planar Misclosure**

Measurement residuals from the adjustment were also examined. Figure 6-7 shows a nearly normal distribution in residuals from the range and horizontal angle measurements.

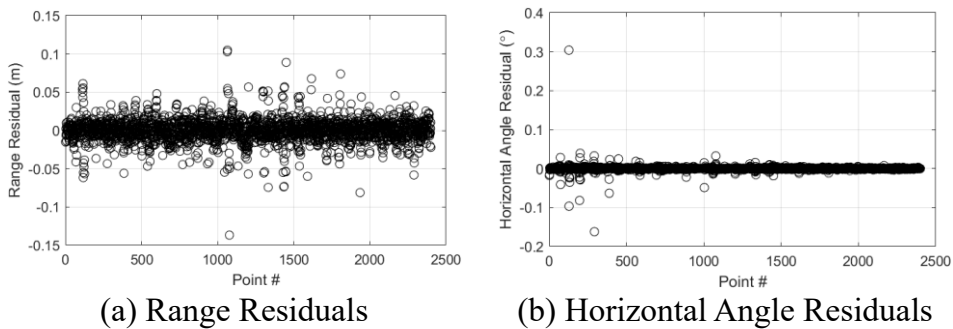


**Figure 6-7. Residuals of the Adjustment**

Furthermore, the reliability of the estimated parameter can be presumed by examining the correlation coefficients between the estimated parameters. The highest correlation coefficient was recorded at a value of

0.868 between scale factor and distance offset (Table 6-5). This result is consistent when compared to the simulation experiment in Section 6.1, indicating that the adjustment was relatively successful. Overall correlations were lower than that of the simulation experiment. Moreover, statistics of the estimated parameters are given in Table 6-6. The estimated values showed reasonable results when compared to related works in the literature, and the standard deviation of the estimated APs were fairly low.

**Table 6-5.** Averaged Correlation Coefficients Between Estimated Parameters of Calibration R-I

	$X_o$	$Y_o$	$Z_o$	$\omega$	$\phi$	$\kappa$	$S$	$D$	$\Delta\theta$	$\Delta\alpha$
$X_o$	-	0.255	0.292	0.029	0.188	0.230	-	0.045	0.098	0.091
$Y_o$		-	0.483	0.013	0.162	0.008	-	0.043	0.208	0.124
$Z_o$			-	0.305	0.375	0.118	-	0.034	0.203	0.176
$\omega$				-	0.133	0.002	-	0.022	0.633	0.134
$\phi$					-	0.225	-	0.072	0.068	0.066
$\kappa$						-	-	0.172	0.034	0.027
$S$							-	0.868	0.174	0.495
$D$								-	0.171	0.442
$\Delta\theta$									-	0.245
$\Delta\alpha$										-

**Table 6-6.** Statistics of the Estimated Parameters of Calibration R-I

	<i>S</i>	<i>D (m)</i>	$\Delta\theta$ ( <i>deg</i> )	$\Delta\alpha$ ( <i>deg</i> )
Min	0.9940	-0.0151	-0.0029	-0.2618
Max	1.0059	0.0217	0.0005	0.2468
Mean	0.9987	0.0090	-0.0013	-0.0033
$\sigma$	0.0034	0.0073	0.0010	0.0271

## 7. Conclusion

In this study, a self-calibration framework using MMS scan data is presented. First, this research performed calibration tests using simulated datasets under various conditions to analyze the plane-based functional model and to find an optimal acquisition method for the calibration datasets. The accuracy of the estimated parameters was measured by examining and analyzing the conditions of normal matrices, standard deviations of parameters, and the difference between preset values. Based on this preliminary analysis, this thesis proposed a self-calibration framework which was processed using both simulation and real datasets. The proposed self-calibration framework was evaluated by investigating planar misclosure, correlation coefficients, measurement residuals, and the standard deviations of estimated parameters. Results showed an improvement of 98% and 57% in planar misclosure for the simulation and real datasets, respectively. The highest correlation coefficients were approximately 0.85 in both datasets.

This thesis consists of the following contributions. First, a comprehensive analysis of plane-based self-calibration was conducted. Through the comparison of self-calibration under various conditions, this research delineated how to acquire a calibration dataset to perform

accurate *in situ* self-calibration. This research can serve as a guideline for users to perform self-calibration of multi-beam laser scanners to improve the overall accuracy and to generate the geometrical feature of point cloud data for precise mapping or surveying.

Extending from the results of this study, this thesis found the following limitations. Suggested future works are also given with respect to these limitations. First, the proposed framework was limited to an indoor environment where planar features can be found easily. In addition, in order to perform frequent calibration with scan data acquired by an MMS, the user should acquire tilted scan data at the corner of the scanned room or corridor. Second, additional accuracy assessment of calibration parameters, such as measuring the distance between estimated and real planes, is required to verify the performance of the proposed framework.

## References

- Atanacio-Jiménez, G., González-Barbosa, J. J., Hurtado-Ramos, J. B., Ornelas-Rodríguez, F. J., Jiménez-Hernández, H., García-Ramirez, T., & González-Barbosa, R. (2011). LiDAR velodyne hdl-64e calibration using pattern planes. *International Journal of Advanced Robotic Systems*, 8(5), 59.
- Bae, K. H., & Lichti, D. (2007). On-site self-calibration using planar features for terrestrial laser scanners. *Int. Arch. Photogramm. Remote Sens. Spat. Inf. Sci*, 36, 14-19.
- Bosché, F., Ahmed, M., Turkan, Y., Haas, C. T., & Haas, R. (2015). The value of integrating Scan-to-BIM and Scan-vs-BIM techniques for construction monitoring using laser scanning and BIM: The case of cylindrical MEP components. *Automation in Construction*, 49, 201-213.
- Chan, T. O., & Lichti, D. D. (2013, May). Feature-based self-calibration of Velodyne HDL-32E LiDAR for terrestrial mobile mapping applications. *In The 8th International Symposium on Mobile Mapping Technology*, Tainan, Taiwan, 1-3.

- Chan, T. O., Lichti, D. D., & Belton, D. (2015). A rigorous cylinder-based self-calibration approach for terrestrial laser scanners. *ISPRS journal of photogrammetry and remote sensing*, 99, 84-99.
- Chen, T., Dai, B., Liu, D., Song, J., & Liu, Z. (2015, June). Velodyne-based curb detection up to 50 meters away. In *2015 IEEE Intelligent Vehicles Symposium (IV)*, 241-248. IEEE.
- Choi, J. (2014, October). Hybrid map-based SLAM using a Velodyne laser scanner. In *17th International IEEE Conference on Intelligent Transportation Systems (ITSC)*, 3082-3087. IEEE.
- Choi, K. H., Kim, Y., & Kim, C. (2019). Analysis of Fish-Eye Lens Camera Self-Calibration. *Sensors*, 19(5), 1218.
- Chow, J., Ebeling, A., & Teskey, B. (2010). Low cost artificial planar target measurement techniques for terrestrial laser scanning. In *in: Proceedings of the FIG Congress 2010: Facing the Challenges—Building the Capacity*.
- Chow, J. C., Lichti, D. D., & Teskey, W. F. (2010a). Self-calibration of the Trimble (Mensi) GS 200 terrestrial laser scanner. *Proceedings of the International Archives of Photogrammetry, Remote Sensing and Spatial Information Sciences*, 38, 161-166.

- Chow, J., Teskey, W. F., & Lichti, D. (2010b). Self-calibration and evaluation of the Trimble GX terrestrial laser scanner. *In Proceedings of The 2010 Canadian Geomatics Conference and Symposium of Commission I, ISPRS* (Vol. 38).
- Chow, J. C. (2018). Multi-sensor integration for indoor 3D reconstruction. *arXiv preprint arXiv:1802.07866*.
- Chen, C. Y., & Chien, H. J. (2012). On-site sensor recalibration of a spinning multi-beam LiDAR system using automatically-detected planar targets. *Sensors*, 12(10), 13736-13752.
- Cole, D. M., & Newman, P. M. (2006, May). Using laser range data for 3D SLAM in outdoor environments. In *Proceedings 2006 IEEE International Conference on Robotics and Automation, 2006. ICRA 2006.*, 1556-1563. IEEE.
- García-San-Miguel, D. A. V. I. D., & Lerma, J. L. (2013). Geometric calibration of a terrestrial laser scanner with local additional parameters: An automatic strategy. *ISPRS journal of photogrammetry and remote sensing*, 79, 122-136.

- Geiger, A., Lenz, P., & Urtasun, R. (2012, June). Are we ready for autonomous driving? the kitti vision benchmark suite. *In 2012 IEEE Conference on Computer Vision and Pattern Recognition* (pp. 3354-3361). IEEE.
- Glennie, C., & Lichti, D. D. (2010). Static calibration and analysis of the Velodyne HDL-64E S2 for high accuracy mobile scanning. *Remote Sensing*, 2(6), 1610-1624.
- Glennie, C., & Lichti, D. D. (2011). Temporal stability of the Velodyne HDL-64E S2 scanner for high accuracy scanning applications. *Remote Sensing*, 3(3), 539-553.
- Glennie, C. (2012). Calibration and kinematic analysis of the velodyne HDL-64E S2 LiDAR sensor. *Photogrammetric Engineering & Remote Sensing*, 78(4), 339-347.
- Glennie, C. L., Kusari, A., & Facchin, A. (2016). Calibration and stability analysis of the vlp-16 laser scanner. *International Archives of the Photogrammetry, Remote Sensing & Spatial Information Sciences*, 40.

- Gruen, A., & Beyer, H. A. (2001). System calibration through self-calibration. In *Calibration and orientation of cameras in computer vision* (pp. 163-193). Springer, Berlin, Heidelberg.
- Halterman, R., & Bruch, M. (2010, May). Velodyne HDL-64E LiDAR for unmanned surface vehicle obstacle detection. In *Unmanned Systems Technology XII* (Vol. 7692, p. 76920D). International Society for Optics and Photonics.
- Hess, W., Kohler, D., Rapp, H., & Andor, D. (2016, May). Real-time loop closure in 2D LIDAR SLAM. In *2016 IEEE International Conference on Robotics and Automation (ICRA)*, 1271-1278.
- Jozkow, G., Totha, C., & Grejner-Brzezinska, D. (2016). UAS TOPOGRAPHIC MAPPING WITH VELODYNE LiDAR SENSOR. *ISPRS Annals of Photogrammetry, Remote Sensing & Spatial Information Sciences*, 3(1).
- Kukko, A., Kaartinen, H., Hyypä, J., & Chen, Y. (2012). Multiplatform mobile laser scanning: Usability and performance. *Sensors*, 12(9), 11712-11733.

- Lichti, D., Stewart, M. P., Tsakiri, M., & Snow, A. J. (2000). Calibration and testing of a terrestrial laser scanner. *International archives of Photogrammetry and Remote sensing*, 33(B5/2; PART 5), 485-492.
- Lichti, D. D., & Licht, M. G. (2006). Experiences with terrestrial laser scanner modelling and accuracy assessment. *Int. Arch. Photogramm. Remote Sens. Spat. Inf. Sci*, 36(5), 155-160.
- Lichti, D. D. (2007). Error modelling, calibration and analysis of an AM-CW terrestrial laser scanner system. *ISPRS Journal of Photogrammetry and Remote Sensing*, 61(5), 307-324.
- Lichti, D. D. (2010a). A review of geometric models and self-calibration methods for terrestrial laser scanners. *Boletim de ciências geodésicas*, 16(1).
- Lichti, D. D. (2010b). Terrestrial laser scanner self-calibration: Correlation sources and their mitigation. *ISPRS Journal of Photogrammetry and Remote Sensing*, 65(1), 93-102.

- Lichti, D. D., Chow, J., & Lahamy, H. (2011). Parameter de-correlation and model-identification in hybrid-style terrestrial laser scanner self-calibration. *ISPRS Journal of Photogrammetry and Remote Sensing*, 66(3), 317-326.
- Moosmann, F., & Stiller, C. (2011, June). Velodyne slam. In *2011 IEEE Intelligent Vehicles Symposium (IV)*, 393-398.
- Muhammad, N., & Lacroix, S. (2010, October). Calibration of a rotating multi-beam LiDAR. In *2010 IEEE/RSJ International Conference on Intelligent Robots and Systems*, 5648-5653. IEEE.
- Park, H. S., Lee, H. M., Adeli, H., & Lee, I. (2007). A new approach for health monitoring of structures: terrestrial laser scanning. *Computer-Aided Civil and Infrastructure Engineering*, 22(1), 19-30.
- Ravi, R., Lin, Y. J., Elbahasawy, M., Shamseldin, T., & Habib, A. (2018). Bias impact analysis and calibration of terrestrial mobile LiDAR system with several spinning multibeam laser scanners. *IEEE Transactions on Geoscience and Remote Sensing*, 56(9), 5261-5275.

- Reshetyuk, Y. (2009). Self-calibration and direct georeferencing in terrestrial laser scanning (Doctoral dissertation, KTH).
- Riveiro, B., & Lindenberg, R. (Eds.). (2019). Laser Scanning: An Emerging Technology in Structural Engineering (Vol. 14). CRC Press.
- Schnabel, R., Wahl, R., & Klein, R. (2007, June). Efficient RANSAC for point-cloud shape detection. *In Computer graphics forum* (Vol. 26, No. 2, 214-226. Oxford, UK: Blackwell Publishing Ltd.
- Shih, N. J., & Huang, S. T. (2006). 3D scan information management system for construction management. *Journal of construction engineering and management*, 132(2), 134-142.
- Shamseldin, T., Manerikar, A., Elbahnasawy, M., & Habib, A. (2018, April). SLAM-based Pseudo-GNSS/INS localization system for indoor LiDAR mobile mapping systems. In *2018 IEEE/ION Position, Location and Navigation Symposium (PLANS)*, 197-208. IEEE.

- Skaloud, J., & Lichti, D. (2006). Rigorous approach to bore-sight self-calibration in airborne laser scanning. *ISPRS journal of photogrammetry and remote sensing*, 61(1), 47-59.
- Tang, P., Anil, E. B., Akinci, B., & Huber, D. (2011). Efficient and effective quality assessment of as-is building information models and 3D laser-scanned data. In *Computing in Civil Engineering (2011)*, 486-493.
- Velodyne, 2019, Velodyne VLP-16 user's manual. <  
[https://go.pardot.com/1/208822/2018-02-23/6t1jp?File\\_Name=ManualVLP16&File\\_Code=ManualVLP16](https://go.pardot.com/1/208822/2018-02-23/6t1jp?File_Name=ManualVLP16&File_Code=ManualVLP16)  
>
- Wu, Y., Kim, H., Kim, C., & Han, S. H. (2009). Object recognition in construction-site images using 3D CAD-based filtering. *Journal of Computing in Civil Engineering*, 24(1), 56-64.
- Yang, H., Xu, X., & Neumann, I. (2015). Laser scanning-based updating of a finite-element model for structural health monitoring. *IEEE Sensors Journal*, 16(7), 2100-2104.

## 국문 초록

LiDAR (Light Detection and Ranging) 센서는 대규모 환경에 대한 정확한 3D 정보를 효율적으로 취득한다. 또한 최근 센서의 발전에 따라, LiDAR 센서는 점차 소형화되며 휴대성이 증가하여 모바일 매핑, 자율주행차 등과 같은 모바일 애플리케이션에 적용될 수 있는 기회가 증대되었다. LiDAR 센서 중, 멀티빔 레이저 스캐너는 지상 레이저 스캐너에 비해 가격이 저렴하고 크기가 작다는 장점이 있어 모바일 애플리케이션에 주로 활용된다.

하지만, 멀티빔 레이저 스캐너는 요구 정확도가 높은 모바일 매핑 애플리케이션에 효과적으로 사용되기에는 상대적으로 정확도가 낮다. 또한, 멀티빔 레이저 스캐너는 관측 값에 대한 불안정성을 나타내는 것으로 연구된 바 있다. 이러한 한계를 극복하기 위해 다양한 연구에서 셀프캘리브레이션을 수행하여 3D RMSE를 센티미터 이하로 줄인 바 있으나 멀티빔 레이저 스캐너의 불안정성에 따라 높은 정확도를 유지하기 위해서는 주기적인 캘리브레이션이 필수적이라 할 수 있다. 따라서 높은 정확도를 요구하는 모바일 애플리케이션에 사용하기 위해서는 데이터 수집 중 주기적인 현장 셀프캘리브레이션이 필요하다.

본 논문에서는, MMS (Mobile Mapping System)에 의해 획득된 스캔 데이터를 사용하여 멀티빔 레이저 스캐너의 지속적이고 주기적인 현장 셀프캘리브레이션의 프레임 워크를 제안한다. 이를 위해, 먼저 평면 기반 셀프캘리브레이션의 분석을 수행하였다. 다음으로, 캘리브레이션 파라미터의 함수 종속성을 분석한 후 실험을 설계하였다. 조정 시 평면

의 크기와 개수, 네트워크 지오메트리 등 다양한 조건의 시뮬레이션 실험 결과 분석을 통해 현장 셀프캘리브레이션 프레임 워크를 제안하였으며 시뮬레이션 및 실제 데이터셋을 사용하여 정확성을 검증하였다.

실험 결과, 약 57%의 RMSE가 감소하였으며 정확한 현장 셀프 캘리브레이션을 수행하기 위한 캘리브레이션 데이터셋의 취득 지침을 제공함으로써 사용자의 현장 셀프 캘리브레이션의 효율성과 정밀성을 향상시킬 수 있을 것으로 판단된다. 또한, 지속적이고 주기적인 현장 캘리브레이션을 통해 효율적이고 정확한 포인트 클라우드 데이터를 획득할 수 있을 것으로 판단된다. 제안 방법은 향후 실내 모바일 매핑 상황과 같은 모바일 매핑 데이터 취득 도중 실시간 캘리브레이션을 통하여 정확한 모바일 매핑을 수행하는데 도움이 될 것으로 판단된다.

**주요어:** 라이다, 셀프캘리브레이션, 멀티빔레이저스캐너, 모바일매핑시스템

**학번:** 2018-24869